Analytical model for Joule-Thomson cooling under heat exchange during CO_2 storage

Chesnokov, Christina; Farajzadeh, Rouhi; Prempeh, Kofi Ohemeng Kyei; Kahrobaei, Siavash; Snippe, Jeroen; Bedrikovetsky, Pavel

DOI
10.1016/j.advwatres.2024.104758

Publication date
2024

Document Version
Final published version

Published in
Advances in Water Resources

Advances in Water Resources 190 (2024) 104758

Contents lists available at ScienceDirect

Advances in Water Resources

journal homepage: www.elsevier.com/locate/advwatres

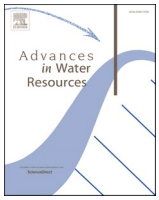

Analytical model for Joule-Thomson cooling under heat exchange during CO_2 storage

Christina Chesnokov [a], Rouhi Farajzadeh [b,c], Kofi Ohemeng Kyei Prempeh [a], Siavash Kahrobaei [b], Jeroen Snippe [b], Pavel Bedrikovetsky [a,*]

[a] The University of Adelaide, Adelaide, SA, Australia
[b] Shell Global Solutions International, The Hague, the Netherlands
[c] Delft University of Technology, Delft, the Netherlands

ARTICLE INFO

Keywords:
CO_2 storage
Joule-Thomson
Heat exchange
Newton's law
Analytical model
Aquifer

ABSTRACT

This paper discusses axi-symmetric flow during CO_2 injection into a non-adiabatic reservoir accounting for Joule-Thomson cooling and steady-state heat exchange between the reservoir and the adjacent layers by Newton's law. An exact solution for this 1D problem is derived and a new method for model validation by comparison with quasi 2D analytical heat-conductivity solution is developed. The temperature profile obtained by the analytical solution shows a temperature decrease to a minimum value, followed by a sharp increase to initial reservoir temperature on the temperature front. The temperature distribution head of the front is determined by the initial reservoir temperature, while the solution behind the front is determined by the temperature of injected CO_2. The analytical model exhibits stabilisation of the temperature profile and the cooled zone. The explicit formula for temperature distributions allows determining the maximum injection rate that avoids hydrate formation.

1. Introduction

The growing concerns over negative impacts of greenhouse gases, in particular Carbon dioxide (CO_2), on climate change have increased the interest in developing different methods to reduce their emissions into the atmosphere. A practical and complementary solution is to capture CO_2 from highly concentrated sources, e.g., industrial plants or directly from air and store it in underground geological formations such as depleted oil and gas reservoirs, deep saline aquifers, and coal beds.

Depleted gas fields exhibit several advantages over other geological formations. The extracted gas from these fields can in principle be replaced by CO_2 and as such, huge volumes of CO_2 can be stored in these reservoirs. For example, it has been estimated that in the Dutch sector of the North Sea, theoretically, more than 1.5 Gton of CO_2 can be stored in the depleted gas fields (Van der Velde et al., 2008). Due to large recovery factors (extracted fraction of the initial volumes) and compressibility of gas more space is available in the gas fields compared to oil fields, in which the extracted oil is usually replaced by injection of another (usually incompressible) fluids (Hamza et al., 2021).

The production of oil fields often involves injection of external fluids (for pressure maintenance or improved-recovery purposes) and/or drilling of a much larger number of wells, limiting the storage volumes of CO_2 and increasing the risk of leakage pathways (Van der Velde et al., 2008). Compared to aquifers, because of their long production history, the uncertainty in the geological settings (permeability, heterogeneity, faults, fractures, etc.) of the hydrocarbon fields is relatively low. Moreover, these fields have proven seal and containment integrity and have part of the infrastructure required to handle the gas. The sequestration of CO_2 can also be combined with enhancing gas recovery, which could partially compensate for the cost associated with CO_2 sequestration (Battashi et al., 2022; Hamza et al., 2021).

However, there are challenges with CO_2 storage in depleted gas reservoirs, some of which are related to the thermodynamic properties of CO_2. From point of capture (or production) to inside the reservoir pores, CO_2 experiences different pressure and temperature conditions and may exist in gas, liquid or, under certain conditions, solid forms. Of particular concern for CO_2 storage in low-pressure reservoirs is the so-called Joule-Thomson (J-T) cooling effect, which is caused by expansion of CO_2 from high surface pressures to low reservoir pressures.

This is schematically shown by path $A \rightarrow D$ in Fig. 1. Point A represents the pressure and the temperature of the transported CO_2 at the storage site, which is assumed to be at 100 bar and 30 °C (i.e., CO_2 is injected in dense liquid phase). With the assumptions that heat

* Corresponding author.
E-mail address: pavel.bedrikovetski@adelaide.edu.au (P. Bedrikovetsky).

https://doi.org/10.1016/j.advwatres.2024.104758
Received 3 January 2024; Received in revised form 30 May 2024; Accepted 17 June 2024
Available online 18 June 2024

Nomenclature

a_a	Thermal diffusivity of adjacent formations m^2/s
A	Dimensionless J-T coefficient[-]
A^*	Dimensionless J-T number[-]
B	Dimensionless heat exchange flux[-]
C	Dimensional heat exchange parameterm^{-2}
c_s	Heat capacity of reservoir rockJ/kg/K
c_w	Heat capacity of waterJ/kg/K
c_f	Heat capacity of CO_2J/kg/K
c_{sa}	Heat capacity of adjacent formation rock J/kg/K
D	Dimensional J-T number for steady state case K m
h	Formation thickness m
k	Formation absolute permeability m^2
K_{rgwi}	End-point relative permeability of CO_2 [-]
l	Shale thickness m
M_j	Mass injection rate kg/s
p	Fluid pressure Pa
p_w	Well pressure Pa
p_e	Reservoir pressure Pa
P_{min}	Pressure at minimum reservoir temperature Pa
q	CO_2 injection rate m^3/s
r	Radial distance along flow direction m
r_w	Well radius m
r_f	CO_2 front position m
r_{norm}	Normalized distance [-]
R_j	Injection radius m
r_p	Temperature penetration depth m
r_{min}	Distance at minimum temperature m
S_{wi}	Connate water saturation [-]
T	Temperature K
T_I	Initial reservoir temperature K
T_J	Injection temperature K
T_D	Dimensionless reservoir temperature [-]
T_{min}	Minimum reservoir temperature K
t	Time s
t_j	Injection time s
t_D	Dimensionless time [-]
V^*	Dimensionless temperature front velocity [-]
x_D	Dimensionless distance [-]
x_{wD}	Dimensionless point of injection [-]
x	Spatial integral variable [-]
x_c	Critical distance of validity [-]
z	Vertical coordinate m
z_D	Dimensionless vertical coordinate [-]

Greek letters

α_{JT}	Joule-Thomson coefficient K/Pa
γ_a	Overall adjacent layer heat conductivity W/m/K
γ_r	Overall reservoir rock heat conductivity W/m/K
γ_s	Overall shale heat conductivity W/m/K
γ_{sa}	Heat conductivity of adjacent layers W/m/K
γ_{ss}	Heat conductivity of shale W/m/K
γ_w	Heat conductivity of water W/m/K
ε_T	Dimensionless reservoir heat conductivity [-]
λ	Dimensional temperature front velocity m^{-1}
θ	Dimensionless temperature in vertical heat conduction [-]
κ	Overall heat transfer coefficient of shale $W/m^2/K$
μ_f	Viscosity of CO_2 Pa s
ξ	Dimensional heat exchange term m^{-3}
ρ_s	Reservoir rock density kg/m^3
ρ_w	Water density kg/m^3
ρ_f	CO_2 density kg/m^3
ρ_{sa}	Adjacent layers rock density kg/m^3
ς	Scaled dimensionless time [-]
τ	Temporal integral variable [-]
φ	Reservoir porosity [-]
φ_s	Shale porosity [-]
φ_a	Adjacent layers porosity [-]
ω	Dimensionless parameter [-]

Acronyms

1D	One dimensional
2D	Two dimensional
BC	Boundary condition
IC	Initial condition
JT	Joule Thomson
ODE	Ordinary differential equation
PDE	Partial differential equation
PVI	Pore volume injected
RHS	Right hand side

conduction in the wellbore is negligible and that the viscous and gravity forces balance each other, the bottom-hole pressure of CO_2 is assumed to be close to that of point A (although in practice, the downhole temperature of CO_2 will be slightly higher due to heat conduction from the well, and CO_2 will most likely be in two phase regime). Isenthalpic expansion of CO_2 from 100 bar to a reservoir pressure of 20 bar (point D) reduces the CO_2 temperature to -10 °C. In general, for reservoirs with pressures lower than 35 bar J-T cooling effect reduces the CO_2 temperature to sub-zero values, as illustrated in Fig. 1. This can potentially lead to the formation of hydrates and freezing of pore water, as implied from the pressure-temperature diagram of the water/CO_2 system in Fig. 2a. Here arrows correspond to temperature and pressure profiles, $T(r)$ and $p(r)$, at some moment; the arrows start at well conditions and end up at the reservoir conditions; entering the hydrate zones indicates the solid phase appearance. The near-wellbore appearance of hydrates or ice can in turn result in the impairment of well injectivity and/or loss of well-related containment (Vilarrasa and Rutqvist, 2017). Moreover, the thermal stress generated by the cooling effect can lead to fracturing of the rock, the extent of which needs further investigation. An alternative solution will be to heat CO_2 before injection (path $A \rightarrow B \rightarrow C$ in Fig. 1); however, this method is energy (and CO_2) intensive and adds further to the cost of CO_2 storage. Injection of CO_2 in gas form is also not desirable because storing similar mass rates of CO_2 require the drilling of multiple wells and requires a larger pore space.

The long-term and safe storage of CO_2 requires a detailed understanding of the physical, chemical, geo-mechanical and thermal effects caused by the injection of CO_2 in the reservoirs. This includes mobilisation of fines by CO2-water menisci (Chequer et al., 2020), salinity alteration (Othman et al., 2019; Parvan et al., 2021; Yu et al., 2018) hydrate formation (Machado et al., 2023) and salt precipitation (Miri et al., 2015; Moghadasi et al., 2004). In addition, to identify the type of risk associated with cold CO_2 injection and design a mitigation plan, it is crucial to quantify the range of expected temperatures in the depleted gas reservoirs. Oldenburg (2007) found that for a constant injection rate, lower permeability and higher porosity increase the effect of J-T cooling.

Mathias et al. (2010) derived an exact solution for CO_2 injection accounting for J-T cooling into an adiabatic reservoir (i.e., ignoring heat exchange with surrounding formations). This analytical model presents three-zone structure of the flow domain and provides explicit formulae for the temperature and pressure profiles, and position of the temperature front.

This model, like all analytical models, allows for fast calculations for

multivariant sensitivity studies and can benchmark the numerical methods for more complex modelling (Kacimov and Obnosov, 2023a, 2023b; Katzourakis and Chrysikopoulos, 2019; Moreno et al., 2021). The exact solutions meet the main challenge of the inverse problems for reservoir characterization, where the direct solver is used in iterative procedures of minimization of the deviation between direct solution and measured / observed data. Availability of exact solutions significantly accelerates the inverse algorithms. In addition, the existence of exact solutions is usually a consequence of a symmetry in the equation, which regularizes ill posed inverse problems (Vinogradov and Krasil'Shchik, 1999). An example is classical Buckley-Leverett solution of two-phase displacement and associated inverse Welge and JBN methods (Lake, 1989). Exact solution of 1D deep bed filtration problem (Zhang et al., 2018) also yields well posed inverse problems (Alvarez et al., 2005, 2007). These advantages explain numerous studies on the analytical modelling of problems related to CO_2 storage (Ahmadi and Chen, 2019; Celia et al., 2011; Moreno et al., 2021, 2021, 2021; Nguyen et al., 2022; Norouzi et al., 2022).

Heat exchange between the reservoir and the adjacent layers can significantly affect the non-isothermal flow in porous media (Bedrikovetsky, 1993; Lawal, 2020). Nevertheless, an exact solution for CO_2 injection into low-pressure reservoirs or aquifer with Joule-Thomson cooling accounting for this effect is not available. This paper derives an exact solution accounting for heat exchange between the reservoir and adjacent layers.

The explicit formulae for temperature and pressure allow predicting the timely evolution of the temperature profile, including well injectivity index, and formation damage due to CO_2 cooling. The solution shows that the temperature profile stabilizes with time and the temperature front stops propagating. We introduce the definition of the temperature penetration depth and show its stabilization over time. The analytical solution also allows calculating maximum injection rate that avoids formation of hydrates due to Joule-Thomson cooling, i.e. the paths well-reservoir in Temperature-Pressure (*T-P)* phase diagram that does not enter the hydrate phase domain (Fig. 2). Thedeveloped validation technique compares Newton's heat flux with the exact solution of quasi 2D heat conductivity problem. This defines the validity domain for Newton's law of heat exchange with surrounding formations.

The structure of the paper is as follows. Section 2 describes the major model assumptions and presents the mathematical model and the governing equations. Section 3 presents the explicit solution of the problem, derived in Appendix A. Section 4 calculates for the area of validity of the model using the solution of "vertical" heat conductivity problem derived in Appendix B. Section 5 presents the results of the analytical modelling with engineering applications. Section 6 performs the sensitivity study of the model. Section 7 discusses the model validity and possible extensions. Section 8 concludes the work.

2. Mathematical model

This section presents the mathematical model for temperature profile evolution during CO_2 injection: the model assumptions (Section 2.1) and derivation of the heat-transfer equation (Section 2.2).

2.1. Model assumptions

The main assumptions of the model are: (i) 1D radial unsteady-state single-phase flow in an infinite homogeneous reservoir with thin impermeable shales at the top and the bottom of the reservoir; (ii) the temperature of the injected CO_2 in the wellbore is constant T_J [K]; (iii) CO_2 is injected at a constant rate of q [M^3T^{-1}]; (iv) water, CO_2, and rock are incompressible; (v) density and viscosity of fluids are constant; (vi) Joule-Thomson coefficient, permeability, porosity, heat conductivity and heat capacity of rock and fluids are constant; (vii) water evaporation into gaseous phase is neglected; (viii) heat exchange between the injected CO_2, water, and the rock occurs instantly, i.e. the temperatures of those three phases are equal; (ix) the heat transfer due to conduction in the flow direction is ignored compared to advection; (x) the reservoir contains water with an initial water saturation $S = 1$; (x) piston-like displacement of water by CO_2 resides constant saturation S_{wi} of immobile water behind the displacement front; (xi) steady-state temperature distribution takes place in shales; (xii) temperature at outer boundaries of under- and overburden shales is equal to initial temperature T_I.

Assumption (i) corresponds to common geological setting around the

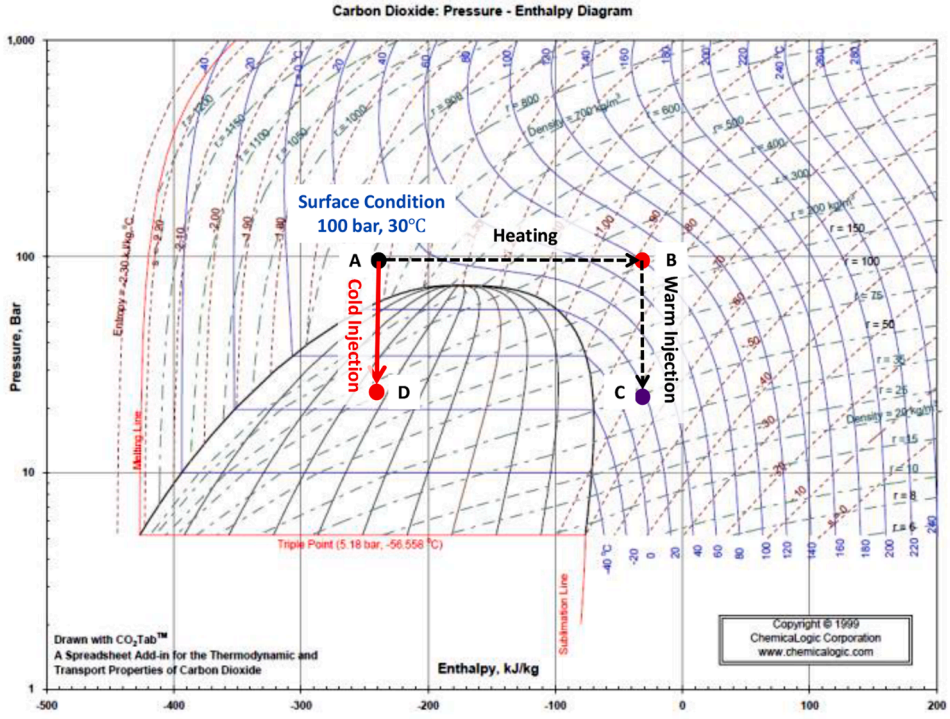

Fig. 1. Pressure-enthalpy diagram of CO_2; the lines with constant temperature are given in blue.

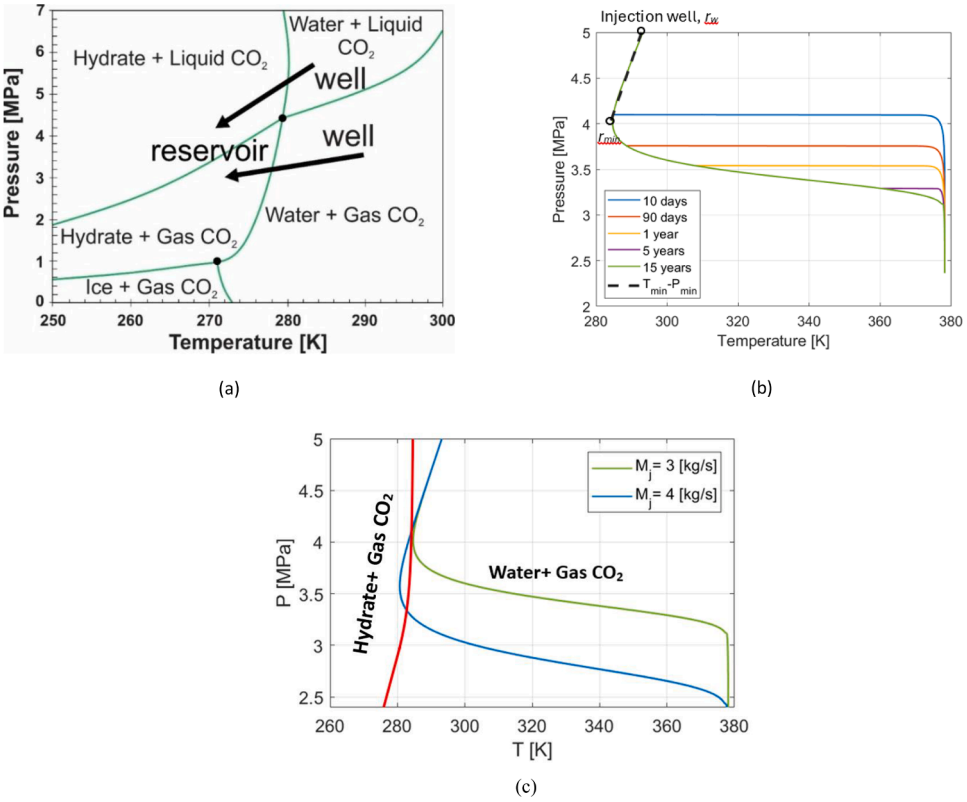

Fig. 2. (a) Pressure-Temperature phase diagram of water-CO_2 binary system, reproduced from *Voronov* et al. *(2016)*, (b) (P,T) diagram based on our model. (c) Mass injection rate effect on a (P,T) diagram, at time $t_D = 1$.

vertical well. Assumptions (ii) and (iii) are usual injection conditions. In the majority of cases, pressure drawdown is significantly smaller than the reservoir pressure, which yields the assumptions (iv, v, vi). Under low equilibrium vapour concentration in CO2, mass of water in aqueous phase is significantly higher than that in gas phase, which justifies assumption (vii). At core scale, the time of heat exchange between the phases is significantly lower than the time of 1 PVI (pore volume injected), so the assumption (viii) is valid. At large scale approximation, the heat convective flux is significantly lower than the heat advective flux, which determines the assumption (ix). Piston-like displacement (x) is common assumption where the phase recovery is not important; this limitation is discussed further in section 7. The assumptions (i)-(x) are common for 1D models of flow in porous reservoirs (Bedrikovetsky, 1993; Lake, 1989; Mathias et al., 2010).

The time of heat conduction through thin shales is significantly lower than the time of 1 PVI, which justifies assumption (xi). The assumption (xii) is valid where the ratio between heat conductivity and heat capacity of dense low-permeability surrounding rocks is significantly lower than that for the reservoir; it justifies using Newton's law of heat conductivity (xii).

Newton's law for the heat exchange between the reservoir and the adjacent layers is a commonly-used assumption for 1D non-isothermal flow models in porous media (Atkinson and Ramey, 1977; Batycky and Brenner, 1997; Fedorov and Sharafutdinov, 1989; Gordeev et al., 1987; Jang et al., 2022; LaForce et al., 2014; Muradov and Davies, 2012, 2009; Payne and Straughan, 1998; Pires et al., 2006; Xu et al., 2013; Yortsos and Gavalas, 1982; Zazovskii, 1983; Zolotukhin, 1979). However, the physical-geological conditions for Newton's law validity are not present in the literature. Derivations in Appendix B present the dimensionless criteria determining the validity of Newton's law. The schematic of the radial problem for CO_2 injection is given in Fig. 3.

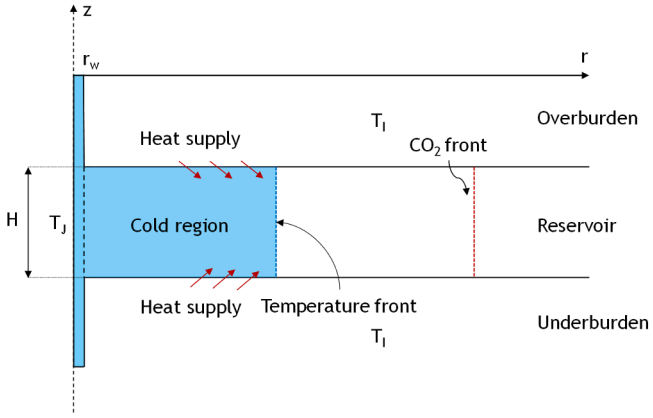

Fig. 3. Schematic of CO_2 injection into a depleted reservoir. The cold part (due to Joule-Thomson cooling effect) is shown in blue.

2.2. 1-D flow equations

The energy-balance equation consists of the accumulation term of heat in the rock, CO_2, and water, advective heat transport, the J-T effect, and heat exchange of the reservoir with the adjacent layers (Gao et al., 2021; Hashish and Zeidouni, 2022; Lake, 1989):

$$2\pi rh\left[(1-\phi)\rho_s c_s + \phi(1-S_{wi})\rho_f c_f + \phi S_{wi}\rho_w c_w\right]\frac{\partial T}{\partial t} + \rho_f c_f q\left[\frac{\partial T}{\partial r} - \alpha_{JT}\frac{\partial p}{\partial r}\right]$$
$$= -2\pi r\frac{\gamma_s(T-T_I)}{l} + h\frac{\partial}{\partial r}\left(2\pi r\gamma_r\frac{\partial T}{\partial r}\right) \quad (1)$$

where ρ_f [ML^{-3}] is density of CO_2, c_f [$L^2T^{-2}K^{-1}$] is the specific heat

capacity of CO_2, ρ_w

[ML^{-3}] is the density of water, c_w [$L^2T^{-2}K^{-1}$] is the specific heat capacity of water, ρ_s [ML^{-3}] is the rock density, c_s [$L^2T^{-2}K^{-1}$] is the rock specific heat capacity, q [L^3T^{-1}] is the injection flow rate, h [L] is the formation thickness, α_{JT} [$M^{-1}LT^2K$] is the J-T coefficient, γ_s and γ_r [$MLT^{-3}K^{-1}$] are the heat transfer coefficients of the shale and reservoir rock, and p [$ML^{-1}T^{-2}$] is the fluid pressure. The unknown in Eq. (1) is the reservoir temperature $T(r,t)$.

The J-T coefficient of CO_2, α_{JT}, depends on the pressure and temperature as shown in Fig. 4. For the depleted reservoirs with pressures of less than 5 MPa, α_{JT} increases with a decreasing temperature. For a fixed temperature, α_{JT} can be assumed independent of pressure for these reservoirs, even though for larger pressures α_{JT} decreases with increasing pressure.

The overall heat transfer coefficient κ [$MT^{-3}K^{-1}$] is defined as:

$$\kappa = \gamma_s l^{-1} \tag{2}$$

It has been experimentally observed that when a fluid with a different temperature than the temperature of the porous medium is injected the heat loss (or gain) per unit length is almost constant. Consequently, the overall heat transfer coefficient, κ, is assumed constant in this study. In other words, the heat conductivity in the z-direction is assumed to be very large, which results in a constant temperature across the vertical thickness of the reservoir (LaForce et al., 2014). However, κ may vary with injection rate, the surface area in contact with surroundings, time, thermal conductivity of the surrounding porous medium, and/or the heat capacity of the reservoir, and the type of process (cold or hot fluid injection) (LaForce et al., 2014). Cold CO_2 injection into a reservoir filled with a hot fluid is analogous to cold water injection in geothermal reservoirs. The experimental data show that for cold water injection lower injection rates are more advantageous for heat extraction from the surrounding rocks.

The volumetric injection rate, q, is defined as:

$$q = M_j \rho_f^{-1} \tag{3}$$

where M_j [MT^{-1}] is the mass injection rate. The position of the CO_2 front r_f [L] is calculated assuming gas incompressibility:

$$M_j t = \pi\left(r_f^2(t) - r_w^2\right)(1 - S_{wi})\phi h \rho_f \tag{4}$$

$$r_f(t) = \left(r_w^2 + \frac{M_j t}{\pi \phi h \rho_f (1 - S_{wi})}\right)^{1/2} \tag{5}$$

Here r_w [L] is well radius.

The pressure gradient in the reservoir is calculated using Darcy's law:

$$\frac{\partial p}{\partial r} = -\frac{\mu_f q}{2\pi r h K_{rgwi} k} \tag{6}$$

where μ_f [$ML^{-1}T^{-1}$] is viscosity of CO_2, K_{rgwi} is the end-point relative permeability of CO_2 and k[L^2] is reservoir rock permeability. Finally, the substitution of Eq. (6) into Eq. (1) yields:

$$\frac{\partial T}{\partial t} + \frac{\rho_f c_f}{\left[(1-\phi)\rho_s c_s + \phi(1-S_{wi})\rho_f c_f + \phi S_{wi}\rho_w c_w\right]h}\frac{q}{2\pi r}\frac{\partial T}{\partial r} + \frac{\alpha_{JT}\rho_f c_f}{\left[(1-\phi)\rho_s c_s + \phi(1-S_{wi})\rho_f c_f + \phi S_{wi}\rho_w c_w\right]h}\frac{q}{2\pi r}\frac{\mu q}{2\pi r h K_{rgwi} k} =$$
$$-\frac{1}{\left[(1-\phi)\rho_s c_s + \phi(1-S_{wi})\rho_f c_f + \phi S_{wi}\rho_w c_w\right]h}\frac{\gamma_s(T-T_I)}{l} + \frac{1}{\left[(1-\phi)\rho_s c_s + \phi(1-S_{wi})\rho_f c_f + \phi S_{wi}\rho_w c_w\right]h}\frac{h}{2\pi r}\frac{\partial}{\partial r}\left(2\pi r \gamma_r \frac{\partial T}{\partial r}\right) \tag{7}$$

By introducing dimensionless variables:

$$t_D = \frac{t}{t_j};\ T_D = \frac{T}{T_I};\ \ x_D = \frac{\pi\phi h(1-S_{wi})}{q t_j} r^2 = \frac{r^2}{R_j^2};\ x_{wD} = \frac{r_w^2}{R_j^2} \tag{8}$$

where t_j [T] is injection time and R_j [L] is injection radius.

Eq. (7) takes the following form:

$$\frac{\partial T_D}{\partial t_D} + \frac{\rho_f c_f \phi(1-S_{wi})}{\left[(1-\phi)\rho_s c_s + \phi(1-S_{wi})\rho_f c_f + \phi S_{wi}\rho_w c_w\right]}\frac{\partial T_D}{\partial x_D} + \frac{\alpha_{JT} q \mu \rho_f c_f \phi(1-S_{wi})}{\left[(1-\phi)\rho_s c_s + \phi(1-S_{wi})\rho_f c_f + \phi S_{wi}\rho_w c_w\right]4T_I \pi h K_{rgwi} k}\frac{1}{x_D} =$$
$$-\frac{\gamma_s t_j}{\left[(1-\phi)\rho_s c_s + \phi(1-S_{wi})\rho_f c_f + \phi S_{wi}\rho_w c_w\right]lh}(T_D - 1) + \frac{4\pi\phi h(1-S_{wi})\gamma_r}{\left[(1-\phi)\rho_s c_s + \phi(1-S_{wi})\rho_f c_f + \phi S_{wi}\rho_w c_w\right]q}\frac{\partial}{\partial x_D}\left(x_D \frac{\partial T_D}{\partial x_D}\right) \tag{9}$$

Let us estimate dimensionless group in front of heat conductivity term in right-hand side (RHS) of Eq. (9).

$$\varepsilon_T = \frac{4\pi\phi h(1-S_{wi})\gamma_r}{\left[(1-\phi)\rho_s c_s + \phi(1-S_{wi})\rho_f c_f + \phi S_{wi}\rho_w c_w\right]q} \tag{10}$$

The typical intervals for variation of the parameters from RHS of Eq. (10) are presented in Section 4.2. This allows calculating minimum, mean, and maximum values of ε_T, which are 3×10^{-11}, 1×10^{-8}, and 6×10^{-7}, respectively. For those values of $\varepsilon_T << 1$, the heat conductivity flux is significantly smaller than the advective heat flux, allowing its neglecting. This is a typical approximation of governing system of equations with dissipative and non-equilibrium effects (diffusion, viscosity, kinetics) yielding hyperbolic conservation laws with advective fluxes only (Bedrikovetsky, 1993; Polyanin and Zaitsev, 2003). This supports the assumption of negligible heat conductivity in the flow direction mentioned in Section 2.1.

Eq. (9) takes the form:

$$\frac{\partial T_D}{\partial t_D}+\frac{\rho_f c_f \phi(1-S_{wi})}{\left[(1-\phi)\rho_s c_s+\phi(1-S_{wi})\rho_f c_f+\phi S_{wi}\rho_w c_w\right]}\frac{\partial T_D}{\partial x_D}+\frac{\alpha_{JT} q\mu\rho_f c_f \phi(1-S_{wi})}{\left[(1-\phi)\rho_s c_s+\phi(1-S_{wi})\rho_f c_f+\phi S_{wi}\rho_w c_w\right]4T_I\pi h K_{rgwi}k}\frac{1}{x_D}=$$
$$-\frac{\gamma_s t_j}{\left[(1-\phi)\rho_s c_s+\phi(1-S_{wi})\rho_f c_f+\phi S_{wi}\rho_w c_w\right]lh}(T_D-1) \tag{11}$$

The boundary condition (BC) for Eq. (7) correspond to the injection of CO_2 with a constant temperature:

$$r=r_w: T=T_J \tag{12}$$

The initial condition (IC) corresponds to the equality of the initial temperatures of the main reservoir rock and the adjacent layers, i.e.,

$$t=0: T=T_I \tag{13}$$

Eq. (11) contains three dimensionless groups – V, A, and B:

$$V=\frac{\rho_f c_f \phi(1-S_{wi})}{\left[(1-\phi)\rho_s c_s+\phi(1-S_{wi})\rho_f c_f+\phi S_{wi}\rho_w c_w\right]}$$
$$A=\frac{\alpha_{JT} q\mu\rho_f c_f \phi(1-S_{wi})}{\left[(1-\phi)\rho_s c_s+\phi(1-S_{wi})\rho_f c_f+\phi S_{wi}\rho_w c_w\right]4T_I\pi h K_{rgwi}k} \tag{14}$$
$$B=\frac{\gamma_s t_j}{\left[(1-\phi)\rho_s c_s+\phi(1-S_{wi})\rho_f c_f+\phi S_{wi}\rho_w c_w\right]lh}$$

where temperature front velocity $V<1$ due to microscale heat conduction from the injected gas to rock and connate water, A characterises Joule-Thomson effect, and B relates to heat exchange of the reservoir with surrounding formations.

Eq. (11) takes the form:

$$\frac{\partial T_D}{\partial t_D}+V\frac{\partial T_D}{\partial x_D}+A\frac{1}{x_D}=-B(T_D-1) \tag{15}$$

Introduction of another time scale reduces the number of dimensionless groups in the governing Eq. (15) by one:

$$\frac{\partial T_D}{\partial \varsigma}+V^*\frac{\partial T_D}{\partial x_D}+A^*\frac{1}{x_D}=-(T_D-1),\quad \varsigma=Bt_D \tag{16}$$

Here two independent dimensionless numbers are:

$$V^*=\frac{V}{B};A^*=\frac{A}{B} \tag{17}$$

The BC from Eq. (12) and IC from Eq. (13) in dimensionless form are as follows:

$$x_D=x_{wD}: T_D=\frac{T_J}{T_I} \tag{18}$$

$$\varsigma=0: T_D=1 \tag{19}$$

It is assumed that the heat transfer within the rock occurs instantaneously, i.e., the injected cold CO_2 is instantly heated up by the residing water and rock. This implies that the temperature front lags significantly behind the CO_2 front inside the reservoir.

3. Exact analytical solution

The exact solution of Eq. (16) with initial and boundary conditions Eqs. (18-19) is obtained by the method of characteristics (Polyanin and Nazaikinskii, 2016; Polyanin and Zaitsev, 2003) the derivations are given in Appendix A. The substitution of the dimensionless parameters given by Eqs. (8) and (17) into Eq. (A16) yields the dimensional form of the solution:

$$T(r,t)=\begin{cases} T_I+(T_J+T_I)e^{-\frac{\xi}{\lambda}\pi(r^2-r_w{}^2)}+\dfrac{\alpha_{JT}\mu_f q}{4\pi K_{rgwi}kh}\left[Ei\left(\dfrac{\xi}{\lambda}\pi r_w{}^2\right)-Ei\left(\dfrac{\xi}{\lambda}\pi r^2\right)\right]e^{-\frac{\xi}{\lambda}\pi r^2}; & \dfrac{\pi r^2-\pi r_w{}^2}{q\lambda}<t \\ T_I+\dfrac{\alpha_{JT}\mu_f q}{4\pi K_{rgwi}kh}\left\{Ei\left[\dfrac{\xi}{\lambda}(\pi r^2-\lambda qt)\right]-Ei\left[\dfrac{\xi}{\lambda}\pi r^2\right]\right\}e^{-\frac{\xi}{\lambda}\pi r^2}; & \dfrac{\pi r^2-\pi r_w{}^2}{q\lambda}>t \end{cases} \tag{20}$$

Here, the dimensional constants λ and ξ are:

$$\lambda=\frac{\rho_f c_f}{h\left[(1-\phi)\rho_s c_s+\phi(1-S_{wi})\rho_f c_f+\phi S_{wi}\rho_w c_w\right]} \tag{21}$$

$$\xi=\frac{\kappa}{qh\left[(1-\phi)\rho_s c_s+\phi(1-S_{wi})\rho_f c_f+\phi S_{wi}\rho_w c_w\right]} \tag{22}$$

The analytical model (A16), (20) can be extended for the case where the injected temperature changes with time – $T_J(t_D)$. In this case, T_J in Eq. (A16) must be substituted by $T_J(\varsigma-(x_D-x_{wD})/V^*)$.

Let us define the depth of temperature wave penetration as a coor-

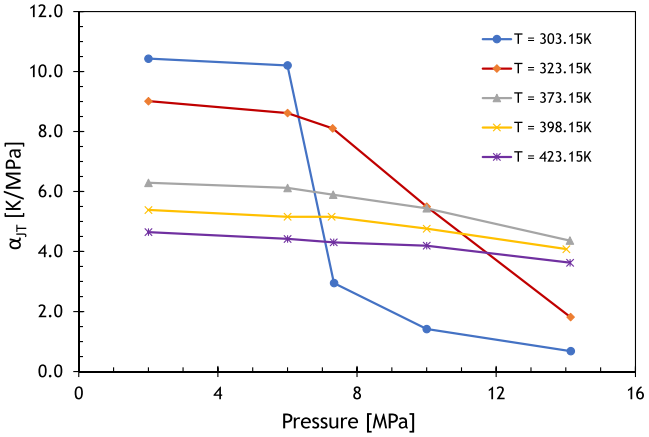

Fig. 4. Joule-Thomson coefficient of CO_2 as a function of pressure for different temperatures (modified from Gao et al. (2021)).

Table 1
Model parameters used in this study.

Parameter	Symbol	Value	Unit
Formation thickness	h	91	m
Porosity	φ	0.11	[-]
Absolute permeability	k	2×10^{-15}	m^2
End point relative permeability	K_{rgwi}	1	[-]
Well radius	r_w	0.1	m
Rock density	ρ_s	2600	kg/m^3
Water density	ρ_w	992	kg/m^3
CO_2 density	ρ_f	141.4	kg/m^3
CO_2 viscosity	μ_f	16.7×10^{-5}	Pa.s
Heat capacity of rock	c_S	1000	J/kg/K
Heat capacity of water	c_w	4037	J/kg/K
Heat capacity of CO_2	c_f	904	J/kg/K
Joule Thomson coefficient	α_{JT}	10.2×10^{-6}	K/Pa
Well pressure	p_w	50×10^5	Pa
Reservoir temperature	T_I	378.15	K
Injection temperature	T_J	293.15	K
CO_2 mass injection rate	M_j	3	kg/s
Connate water saturation	S_{wi}	0.2	[-]

dinate of the "centre" of the wave. For variable r, the probability distribution function can be defined as:

$$F(r) = \frac{(T(r,t) - T_I)r}{\int_{r_w}^{\infty} (T(r,t) - T_I) r dr} \tag{23}$$

The arithmetic mean of distance r is the heat penetration depth:

$$r_p = \int_{r_w}^{\infty} F(r) r dr = \frac{\int_{r_w}^{\infty} (T(r,t) - T_I) r^2 dr}{\int_{r_w}^{\infty} (T(r,t) - T_I) r dr} \tag{24}$$

4. Area of validity of the model

This section discusses the area of validity of the analytical model, including comparison between the solutions for adiabatic and non-adiabatic reservoirs (Section 4.1), formulation of the method of 1D model validation by comparison with 2D solution (Section 4.2), and calculations of validity intervals for the model parameters and independent variables (Section 4.3).

4.1. Comparison with adiabatic model

To validate the developed analytical model, the solution given by Eq. (20) was compared with the results of Mathias et al. (2010) in the limit of no heat transfer between the reservoir and the adjacent layers, i.e., $\kappa \to 0$. The parameters provided in Table 1 are used as a basic case for all calculations in this paper.

Table 2 presents the intervals of variation of parameters. Fig. 5 shows the close agreement between the numerical implementations of two models. The time intervals in Fig. 5 correspond to dimensionless time, t_D = 0.002, 0.004, 0.016, 0.067, 0.33, 0.67, 1, 1.33.

As expected, the temperature front falls behind the CO_2 front because

Table 2
Critical points of the (A^*, V^*, ω) domain.

Vertices	V^*	A^*	ω
1	1.13E-07	2.72E-12	1.56×10^{-1}
2	1.13E-07	5.36E-05	1.56×10^{-1}
3	1.13E-07	5.36E-05	1.48×10^{1}
4	1.13E-07	2.72E-12	1.48×10^{1}
5	3.89E-01	2.72E-12	1.56×10^{-1}
6	3.89E-01	5.36E-05	1.56×10^{-1}
7	3.89E-01	5.36E-05	1.48×10^{1}
8	3.89E-01	2.72E-12	1.48×10^{1}
9	4.09E-04	3.22E-06	9.29

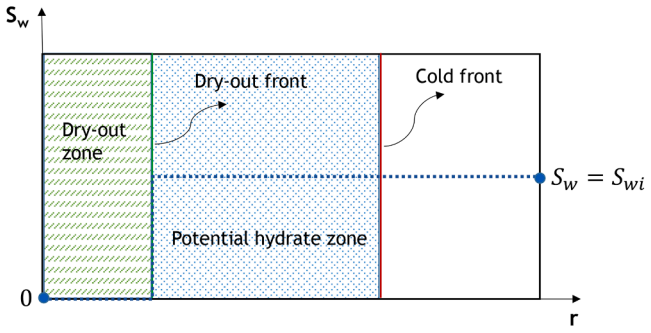

Fig. 6. Formation of a region with a non-zero water saturation between dry-out and cold fronts.

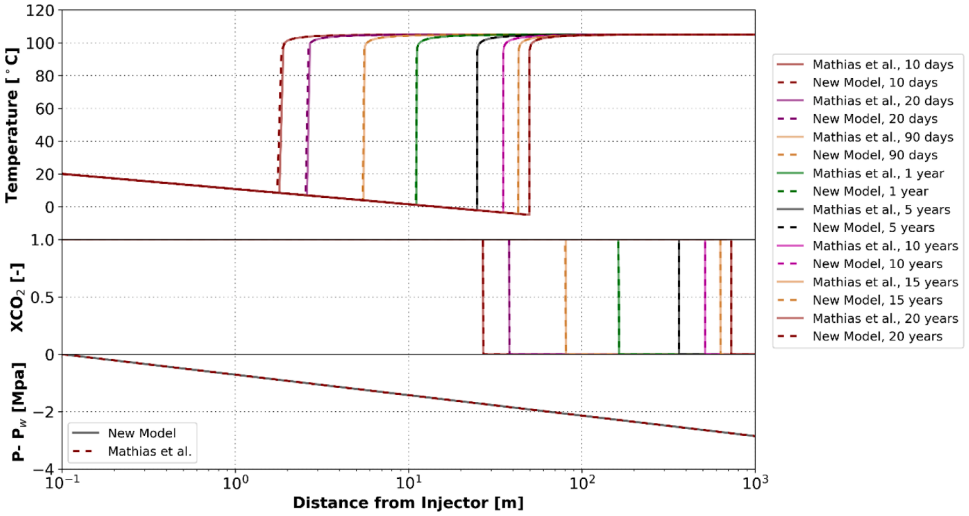

Fig. 5. Comparison of the results of the current model with Mathias et al. (2010) model (κ=0).

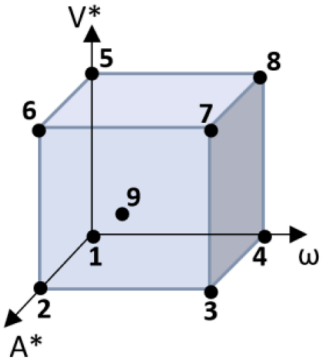

Fig. 7. A tetrahedron defining the domain of the dimensionless numbers A*, V* and ω in the system.

of the heat provided by the rock (the volumetric heat capacity of the rock is much larger than those of both water and CO_2). The temperature decreases from injection temperature to a minimum value and then sharply increases to the initial temperature of the reservoir. There are two distinctive features for the solution of the case, where $\kappa \to 0$: (1) temperature decreases to a minimum value just upstream of the sharp front at each timestep, and (2) the temperature front keeps moving inside the reservoir for as long as CO_2 injection continues. The sharp increase to the initial temperature (shock front) is due to absence of conduction in the analytical model. In accordance with the properties of the radial flow (i.e., large pressure drops near the injection point), the cold front penetrates quickly inside the reservoir. If the injected CO_2 is undersaturated, the residing water in the pores evaporates; and therefore, the water saturation reduces to near-zero close to the injection well. However, the speed of the temperature front is expected to be larger than that of the drying front such that a region with a non-zero water saturation appears between the dry-out and cold fronts in a relatively short time after injection of CO_2. This is schematically shown in Fig. 6. If the pressure and temperature fall within in the hydrate region on the CO_2/water phase diagram in Fig. 2, CO_2 hydrates might form potentially leading to blockage of CO_2 flow.

4.2. Formulating the criterion for validity of Newton's heat exchange

The primary assumption of the model given by Eq. (1) is steady state heat exchange between surrounding formations and impermeable shale that confines the reservoir, which is Newton's law. This section establishes the domain of validity for the heat exchange term used in the energy balance (Eq. (1)), aiming to determine the condition under which the discrepancy between the temperature at the interface, $\theta\ (z_D{=}0,\ t_D)$, and the initial reservoir temperature, $T{=}T_I \to \theta = 1$, is insignificant. In

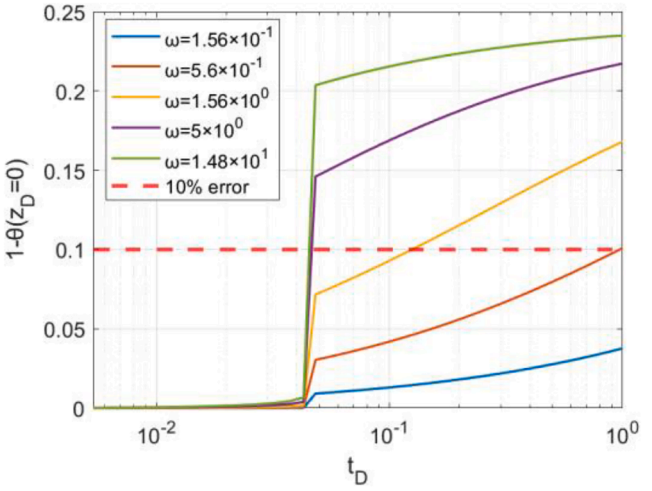

Fig. 9. Newton's law criterion vs. time, for different ω values. Plotted for x_D=4E-5.

our case, we constrain the discrepancy between the two solutions for temperature to the difference of less than or equal to 10 %. Using the solution given by Eq. (20), the heat flux through the shale is determined by the first term in RHS of Eq. (1), which become the inlet boundary condition for "vertical" heat conductivity Eq. (B6). We utilize the solutions obtained for the temperature profile at the interface between adjacent impermeable shale and adjacent formations, as derived in Eq. (B18). The validity condition in dimensionless variables is as follows:

$$1 - \theta(z_D = 0, t_D) < \varepsilon; \varepsilon = 0.1 \tag{25}$$

Newton's law is valid when the temperature on the outer bounds of the adjacent seals is equal to the initial reservoir temperature. This condition depends on conductivity and capacity of the adjacent formation layers i.e., heat conductivity (γ_a) and volumetric heat capacity. Indeed, equality of the temperature on the outer shale bounds to initial reservoir temperature corresponds to ω tending to zero, as defined by Eq. (B8).

The following fluid and rock properties are used to calculate the intervals for parameters *A*, V** and ω. The heat capacities of gas, water and rock varying from 709 J (kg K)$^{-1}$ to 1476 J (kg K)$^{-1}$, 3965 J (kg K)$^{-1}$ to 4335 J (kg K)$^{-1}$ and from 776 J (kg K)$^{-1}$ to 1215 J (kg K)$^{-1}$, respectively. The heat conductivities of shale and adjacent formations ranges from 1 W (m K)$^{-1}$ to 3.7 W (m K)$^{-1}$ and from 3.7 W (m K)$^{-1}$ to 5 W (m K)$^{-1}$, respectively. The densities of gas, water and rock vary from 0.5 kg m^{-3} to 1236 kg m^{-3}, from 527 kg m^{-3} to 1000 kg m^{-3} and from 2270 kg m^{-3} to 3200 kg m^{-3}, respectively. The thicknesses of the

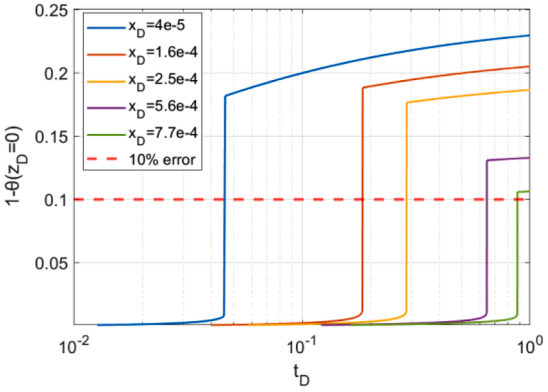

(a)

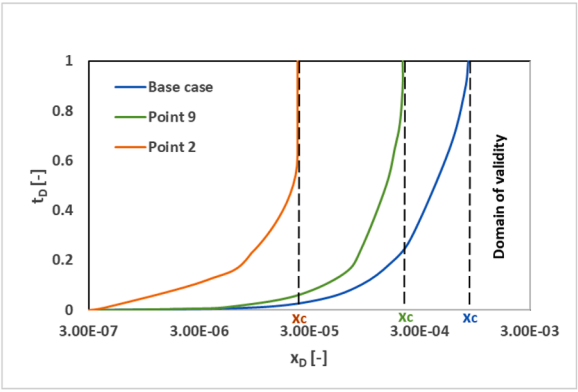

(b)

Fig. 8. Validity of steady state heat exchange (a) validity vs. time for different radii. (b) domain of validity.

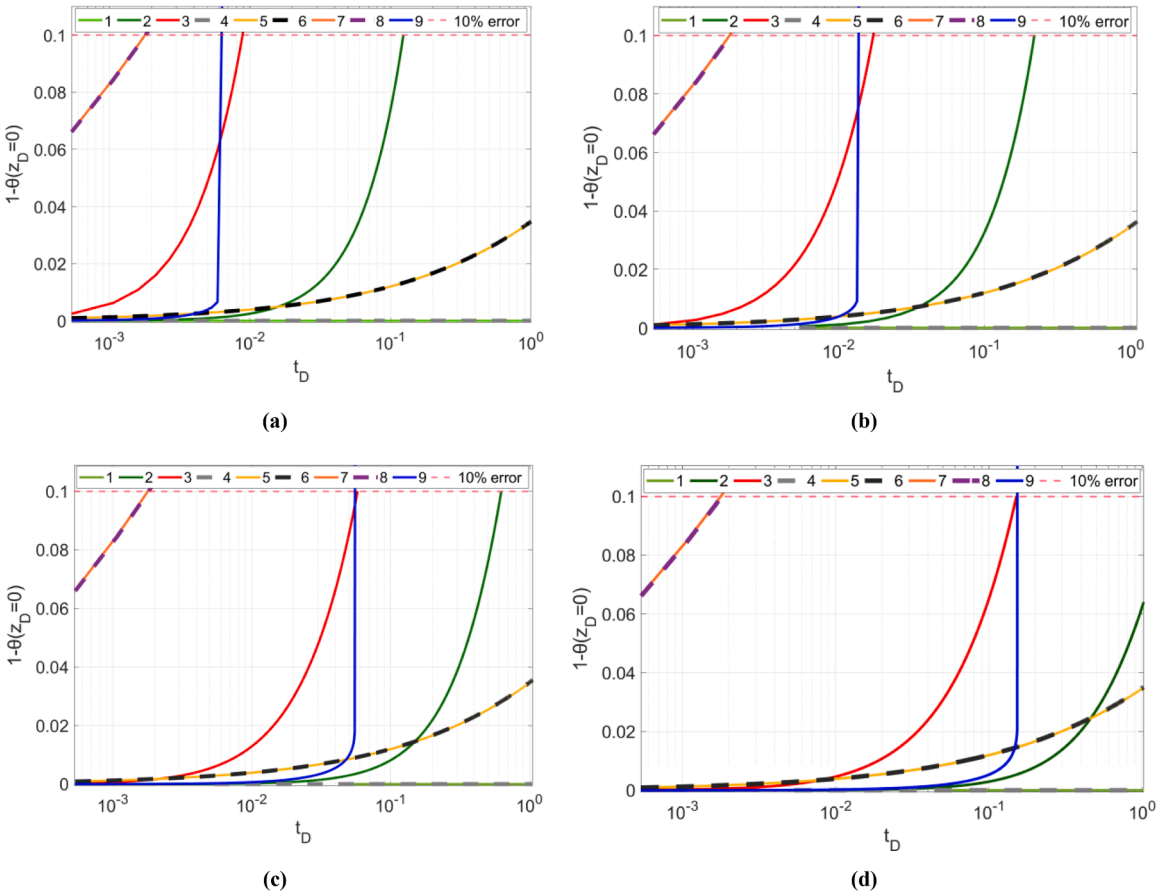

Fig. 10. Difference between temperature on the outer bounds of shale and initial reservoir temperature, to validate Newton's law, temperature history at the distance from injectors at (a) x_D = 2.5E-6, (b) x_D = 5.6E-6, (c) x_D = 2.25E-5, (d) x_D = 6.3E-5.

reservoir and shales vary from 1 m to 100 m and from 1 m to 3.33 m, respectively. Well radius varies from 0.05 m to 0.13 m. Injection rate varies from 0.005 $m^3\,s^{-1}$ to 0.04 $m^3\,s^{-1}$. J-T coefficient varies from 7×10^{-6} K/Pa to 1.1×10^{-5} K/Pa. CO_2 viscosity varies from 1.1×10^{-5} Pa s to 2.7×10^{-4} Pa s. Permeability varies from 3.9×10^{-16} m^2 to 5.9×10^{-14} m^2. The porosity varies from 0.1 to 0.3 and connate water saturation varies from 0.2 to 0.4.

Given that our solution in Eq. (B18) is notably influenced by system parameters- A^*, V^* and ω, a domain made of the three dimensionless numbers, (A^*, V^*, ω) in Eq. (B18) is established. The eight vertices of the tetrahedron 1,2…8 in Fig. 7 correspond to the extreme values of A^*, V^* and ω. The corresponding values of the vortices along with the inner

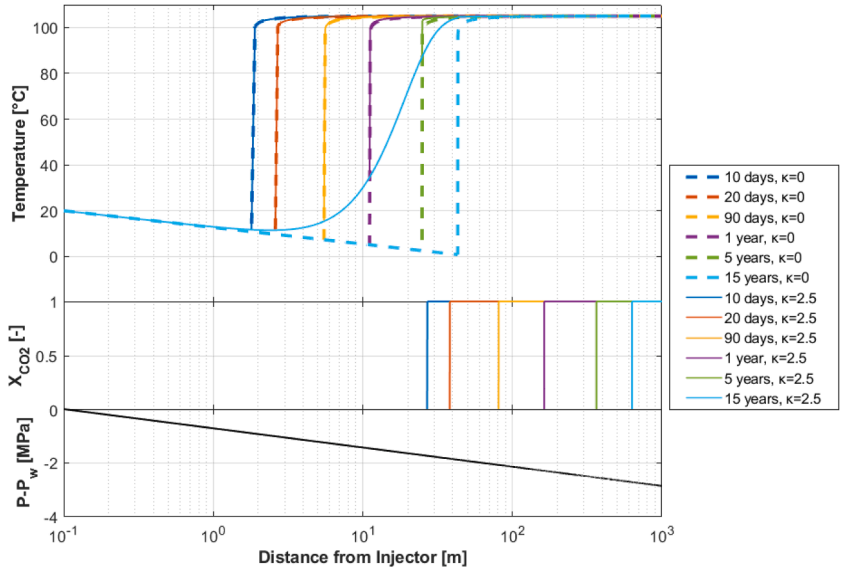

Fig. 11. The impact of heat exchange on temperature profile (solid lines) in comparison to adiabatic system (dashed lines), CO_2 front position and pressure drop for variying times.

point 9 are given in Table 2.

Table 2 summarizes the critical values of the 9 coordinate points illustrated in Fig. 7.

4.3. Determining the area of validity

One of aims of the paper is to determine a region of validity where the condition (Eq. (25)) is upheld. Fig 8-10 visualise the domain of the analytical model validity. Here the injection period is t_j=15 years.

Fig 8a presents the temperature deviation versus time at five distances from the well, which vary from four to seventeen meters. The deviation jumps occur at the temperature front propagating with velocity V^*. The positions of the curves show that the analytical model is valid for radii varying from well radius up to some critical value; this critical value increases with the increase in distance. The model is valid from the beginning of injection up to some time. At 4 m from the well (blue curve) the solution is valid until 0.04 of the injection period. At 17 m, the solution is valid for almost overall injection period (green curve). For larger distances, the solution is valid always.

Fig 8b shows the validity regions below the corresponding critical curves. Here the critical curves correspond to the base case, point 9, and point 2. All critical curves have vertical asymptotes (x_c), meaning that the analytical model at distances larger than x_c is always valid.

Fig. 9 shows how the validity region depends on dimensionless parameter ω. Here the distance from the injector is 4 m. The temperature jump position is the same for all curves since the temperature front is independent of the "vertical" heat conductivity. The lower is the parameter ω, the larger is the validity region. For $\omega > 3.1$, the model is valid before the arrival of temperature front only. For $\omega = 0.156$, the model is valid up to 10 injection periods.

Fig. 10 presents the dimensionless deviation of the temperature on the shale top from the initial temperature and with a 10% cut-off for the nine cases shown in Fig. 7 and Table 2 (cases 1,2…9, respectively). Fig. 10a, b, c, and d correspond to different distances from the injector. For all cases, the part of the temperature deviation profile where the deviation does not exceed 10 % moves to the right and down as the distance grows. This means that the time interval of the model validity increases. The model is valid behind the temperature front (dark blue curves) that moves to the right with increasing distance, this points to an increase in the validity domain with increasing distance from the well.

Let us investigate the effects of dimensionless numbers A^*, V^*, and ω, on the model validity. In cases 2 and 3 (in Table 2), A and V^* are the same; dimensionless parameter ω is higher in case 3. The green curves are located to the right of red curves, so a smaller parameter ω results in a larger validity domain, i.e., the higher is the validity period at the same distance from the well, and the larger is the validity distance for a fixed time.

Considering cases 3 and 4 (in Table 2), V^* and ω are unchanged while the dimensionless J-T number, A^* is higher in case 3. From Fig. 10, the grey dashed curves are located to the right of red curves, meaning a smaller J-T number results in a larger validity domain. Furthermore, the red curves for case 3 are to the right of the orange curves for case 7. Here, the dimensionless numbers A^*, and ω are unchanged and the dimensionless temperature front velocity V^* varies. This shows that a higher front velocity results in a smaller validity domain.

5. Results of the analytical modelling

Here we present the analytical modelling results: dynamics of temperature profiles (Section 5.1), determination of the maximum rate threshold where hydrates do not appear (Section 5.2), and calculation of formation damage due to Joule-Thomson cooling (Section 5.3).

5.1. Analysis of temperature profiles

The impact of heat exchange between the main formation and the surrounding rock on the propagation of the temperature front is shown in Fig. 11. A heat transfer coefficient of $\kappa = 2.5$ W/m^2/K was used in the calculations (Cermak and Rybach, 1982; Labus and Labus, 2018; Robertson, 1988; Schoen, 2015). For comparison, Fig. 11 further shows the case of no heat exchange $\kappa \to 0$ with the dashed curves. Initially and for relatively short times, the impact of the heat gain from the surrounding layers is not significant.

However, as CO_2 injection continues, the heat supplied by these layers heats the injected CO_2 and therefore the temperature increases slightly before jumping to the initial temperature of the reservoir. Unlike the case with no heat exchange, the temperature upstream of the shock is not the lowest temperature. Indeed, a key difference is that the position and the value of the minimum temperature remains fixed for all times in the new model. The area between the solid and the dashed curves in Fig. 11 represents the extent of the impact of the heat exchange. The area increases with time and as a result the length of the shock front becomes smaller every timestep, until it disappears completely. This corresponds to the time at which the system reaches steady state, and the temperature front no longer moves. The steady-state solution of Eq. (1), i.e. the ordinary differential equation (ODE), is obtained by separation of variables:

$$T(r) = T_I + (T_J - T_I)e^{-C\pi\left(r^2 - r_w{}^2\right)} + D\left[Ei\left(C\pi r_w{}^2\right) - Ei\left(C\pi r^2\right)\right]e^{-C\pi r^2} \tag{26}$$

Here, C and D are defined as follows:

$$C = \frac{\kappa}{q\rho_f c_f}; D = \frac{\alpha_{JT}\mu_f q}{4\pi K_{rgwi} k} \tag{27}$$

The time intervals in Fig. 11 correspond to dimensionless time, t_D = 0.002, 0.004, 0.016, 0.067, 0.33, 1, respectively. Eqs. (26) and (27) indicate that the position of the steady state temperature depends largely on the injection rate, the volumetric heat capacity of CO_2 and rock properties. The pressure profile under the assumptions of gas incompressibility and constant viscosity is steady state; it is obtained by integration of Eq. (6). The temperature profile in Fig. 11 shows temperature decreases from the well to the temperature front, and then monotonically increases until initial temperature. Minimum temperature is achieved exactly behind the temperature front.

5.2. Determination of minimum rate preventing hydrate formation

The temperature profiles are crucial to determine a maximum injection rate at which hydrate formation does not occur. Fig. 5 and Fig. 11 show that the temperature profiles reach a minimum just behind the

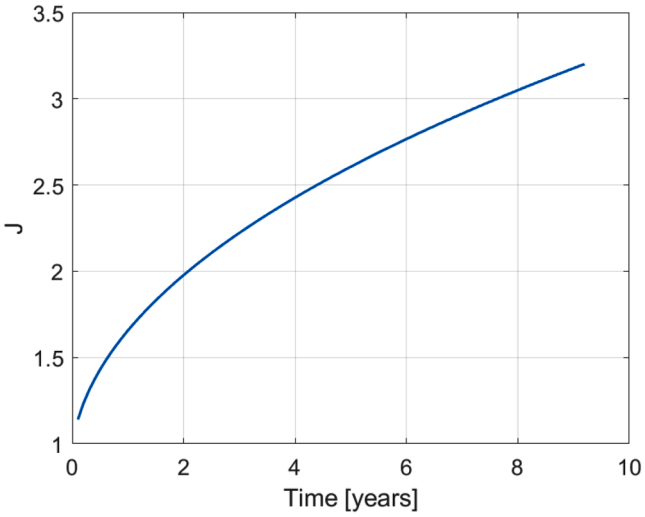

Fig. 12. Pressure drawdown (impedance) versus time

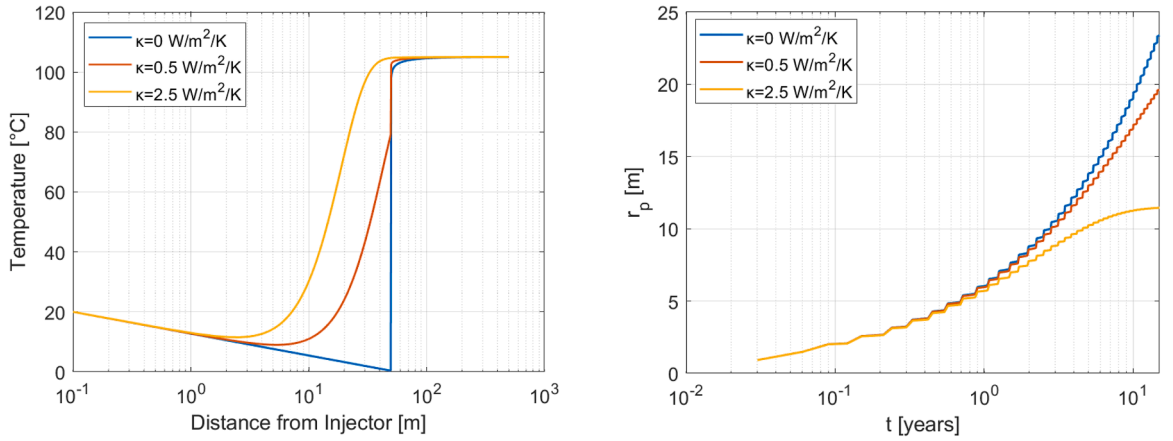

(a) (b)

Fig. 13. (a) The impact of the heat transfer coefficient, κ, on the temperature profile. (b). The impact of the heat transfer coefficient, κ, on the temperature penetration depth.

temperature front. As illustrated by the *T-P* phase diagram in Fig. 2c, the envelope is almost vertical for supercritical CO_2 and is curvilinear at low pressures; hydrate formation does not occur if the well-reservoir arrow does not enter the hydrate phase domain. As it follows from Darcy's law and definition of Joule-Thomson coefficient, both pressure and temperature drops are proportional to the rate q (Eqs. (1) and 6). Therefore, the length of the well-reservoir segment in Fig. 2a is also proportional to injection rate q; the problem is to determine the maximum rate, where the arrow does not cross the hydrate envelope. *T-P* profile at lower mass rate (3 kg/s) touches the envelope curve, while that at higher mass rate (4 kg/s) crosses the envelope and indicates formation of hydrates (Fig. 2c). Fig. 2b shows the well-reservoir path for five moments; all paths must pass outside the envelope to avoid hydrate formation. The pressure profiles are always monotone, while the temperature profiles are not. At high pressures for supercritical CO_2, the envelope is almost vertical, so hydrate formation is controlled by the minimum temperature. The minimum temperate defines a single path $(T(r_{min},t),p(r_{min}))$, shown in Fig. 2b by dashed line; here $r_{min}(t)$ is the radial distance where temperature reaches the minimum point. The explicit formulae for temperature profiles (Eq. (20)) allows calculating the minimum-temperature path:

$$\frac{\partial T}{\partial r}(r_{\min},t)=0,\quad \frac{\partial^2 T}{\partial r^2}(r_{\min},t)>0 \tag{28}$$

From calculation, the profile in the phase diagram almost stabilises after 15 years of injection (green curve in Fig. 2b). The dashed segment of the stabilised curve corresponds to the temperature decline region; its slope is equal to Joule-Thomson coefficient. The dashed segment ends up in the point of temperature minimum during the overall injection period. At the maximum rate that avoids hydrate formation, this point is the touching point between the phase envelope and the stabilised curve.

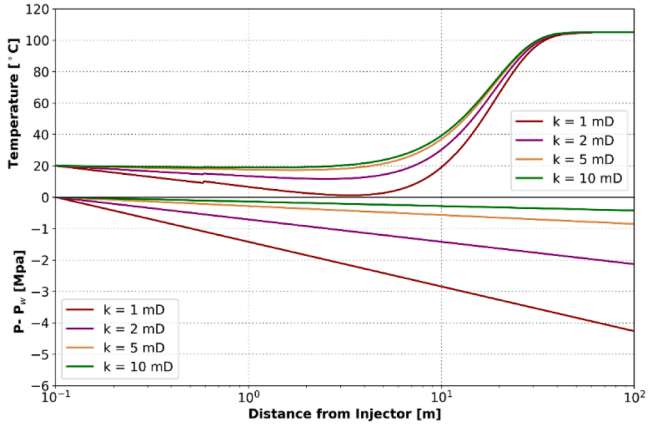

Fig. 14. The impact of permeability on the temperature profiles.

5.3. Joule-Thomson cooling induced formation damage

Consider additional pressure drop on the reservoir under constant injection rate due to CO_2 cooling. Accounting for temperature-dependency of fluid viscosity $\mu_f(T)$, the governing system consists of two Eqs. (1) and (6). Neglecting pressure drawdown outside the displacement zone at the end of injection, i.e., for $r>R_j$, yields the pressure at the displacement front to be equal to the reservoir pressure: $p(r_f(t),t)=p_e$. The unknowns in system (1, 6) are $T(r,t)$ and $p_w(t)$. Assume that viscosity dependency of temperature does not affect the injection rate, i.e., q=const in Eq. (6). Integrating pressure gradient in Eq. (6) in r from r_w to $r_f(t)$, we obtain the expression for pressure drawdown:

$$p(r_w,t)-p\big(r_f(t),t\big)=\frac{q}{2\pi h K_{rgwi}k}\int_{r_w}^{r_f(t)}\frac{\mu_f(T(r,t))dr}{r} \tag{29}$$

The plot of the ratio of the pressure drops (Eq. (29)) at time t and at $t=0$, $J(t)$, is presented in Fig 12. Here we use the following viscosity-temperature correlation (Tsar et al., 2013):

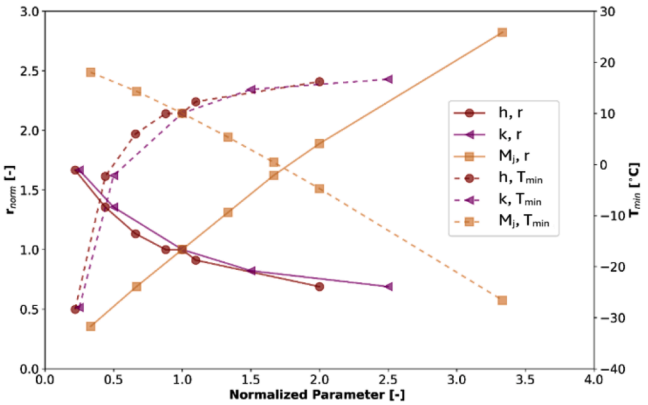

Fig. 15. The impacts of the mass injection, permeability and reservoir thickness on the minimum temperature and the steady-state position of the temperature front in the reservoir. The axes are normalized to the parameters of the base case.

$$\mu_f(T) = 4 \times 10^{-8} T + 3 \times 10^{-6} \quad (30)$$

6. Sensitivity study of the model

This section investigates the sensitivity of the analytical model to the model parameters: heat transfer coefficient (Section 6.1), permeability (Section 6.2), and reservoir thickness as well as injection rate (Section 6.3). Additionally, the effect of the dimensionless numbers A^* and V^* on the temperature profile is investigated in Section 6.4.

6.1. Effect of heat transfer coefficient

The impact of the heat transfer coefficient, κ, is shown in Fig. 13. The temperature profiles are presented for time $t = 20$ years. With the increase of κ, a higher amount of CO_2 is heated and therefore the cold front is retarded, compared to the case where κ is smaller. Moreover, the minimum temperature is slightly lower for the case with the smaller κ, as illustrated in Fig. 13a.

Fig. 13b shows that in the adiabatic reservoir, the penetration depth, which was introduced by Eq. (24), does not stabilize (blue curve). Stabilization of the heat penetration is achieved with the presence of heat exchange in the system. For the given temporal range, the curve corresponding to the lower value for heat conductivity does not stabilize, while the curve corresponding to the higher value achieves stabilization. The three values of heat conductivity presented in Fig. 13 correspond to the following dimensionless numbers- ($A^*, V^* \to \infty$), (A^*=1.8e-5, V^*=4.3e-3), (A^*=3.6e-6, V^*=8.7e-4), respectively.

6.2. Effect of permeability

Fig. 14 shows the sensitivity of the model to varying rock permeabilities. As stated earlier, the magnitude of temperature reduction due to the J-T effect depends on the pressure gradient and the J-T coefficient. For fixed injection pressure and flowrate at the boundary, the pressure gradient increases with decreasing reservoir permeability, causing an increased temperature drop. However, this conclusion is valid only when equal flowrates are considered for different permeabilities. For a heterogeneous reservoir, the injected CO_2 will be distributed in proportion to the permeability of each layer. If the permeability contrast is large, then the large fraction of CO_2 will flow through the high permeability layer causing a larger pressure drop compared to the low-permeability layer. Therefore, for heterogeneous reservoirs with large permeability contrast, the "isenthalpic" expansion of CO_2 will result in lower temperatures in the high permeability layers.

It is worth mentioning that when CO_2 becomes liquid or the pressure exceeds the critical pressure of CO_2 the magnitude of α_{JT} also reduces, especially in the colder regions near wellbore (see Fig. 4) resulting in lower cooling effects. Furthermore, the presence of impurities in the injected CO_2 or contamination of CO_2 with the gas already present in the reservoir will also affect the temperature drop and the extent of the cooling zone (Ziabakhsh-Ganji and Kooi, 2014). Gases like SO_2 expand the cooling zone while gases like N_2 and CH_4 tend to contract this zone (Ziabakhsh-Ganji and Kooi, 2014). The Joule-Thomson cooling effect is more pronounced at low-permeability and thin layers, assuming a constant injection rate. With the increase of the reservoir permeability or thickness the impact becomes less and after a certain value the steady-state temperature profile appears to be independent of these parameters.

The four values of heat conductivity presented in Fig. 14 correspond to the following values of dimensionless numbers A^*: A^*=7.3E-6, A^*=3.6E-6, A^*=1.45E-6, A^*=7.3E-7, respectively.

6.3. Effect of system parameters on minimum reservoir temperature

In the sensitivity analysis shown in Fig. 15, only the investigated model parameter was changed while the other parameters remained constant. For simplicity the parameters are normalized to the parameters of the base-case presented in Table 1. Moreover, the r_{norm} on the y-axis is relative to the position of the steady-state temperature of the base case. The normalized distance has a near linear relationship with the mass injection rate, i.e., the higher the injection rate the longer the cold front travels inside the reservoir. In addition, the minimum temperature significantly decreases as the injection rate increases. For example, with doubling of M_j the minimum temperature drops from 10 °C to −10 °C, which has huge implications on CO_2 storage projects.

6.4. Sensitivity to change in the dimensionless numbers

The dimensionless numbers A^* and V^*, as defined in Eq. (17), are the parameters that account for the J-T effect, and the heat front velocity, respectively. An increase in parameter A^* is equivalent to an increase in the J-T coefficient, injection rate and shale thickness, as well as a decrease in reservoir thickness, shale heat conductivity and permeability. Also, an increase in parameter V^* corresponds to an increase in shale thickness and injection rate, as well as a decrease in shale conductivity.

Fig. 16 show the sensitivity of the temperature profile to the dimensionless numbers, A^* and V^*. From Fig. 16a, it is observed that, while maintaining all other system parameters constant and varying A^*, the temperature drop in the system ranges from $\Delta T = 150$ °C to $\Delta T = 0$.

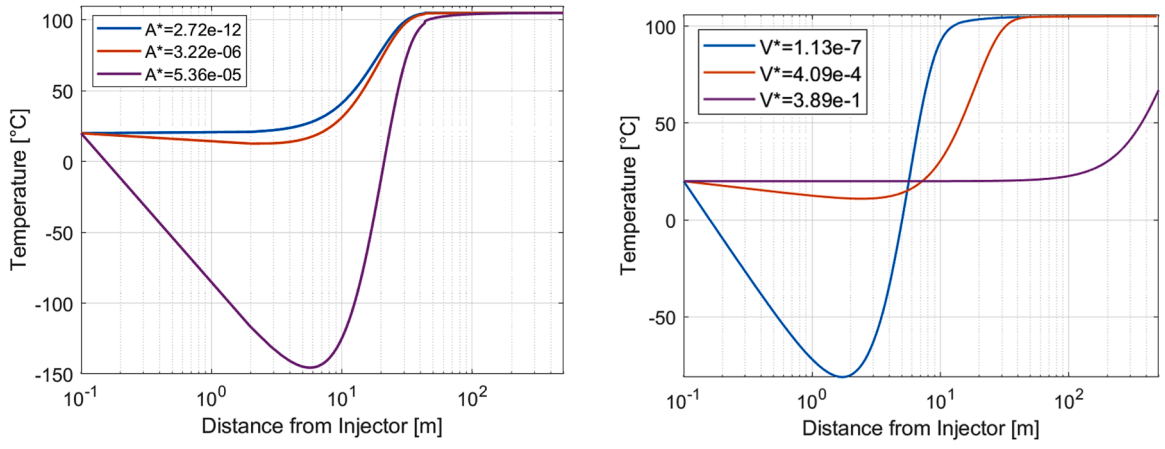

(a) (b)

Fig. 16. Temperature profile sensitivity to (a) A* parameter (b) V* parameter, at time $t_D = 1$.

In Fig. 16b, varying the values of V^*, while holding all other system parameters fixed results to temperature drops varies between $\Delta T = 95\ ^\circ C$ to $\Delta T = 0$. Hence, the system is more sensitive to modifications in parameter A^* when assessing the temperature profiles.

7. Discussion

The exact solution (Eq. (20)) reveals three-zone structure of flow domain, where the temperature distribution behind the temperature front is determined by the injection temperature, and that ahead of the front – by the initial temperature. The solution provides an explicit formulae for temperature distribution $T(r,t)$ allowing for fast calculations of: (i) multivariant sensitivity study, (ii) minimum temperature path in T-P phase diagram; (iii) maximum rate avoiding hydrate formation, (iv) pressure field $p(r,t)$ and the increase in pressure drawdown. From the exact solution follows explicit formulae for (i) trajectory of the temperature front, (ii) temperature jump on the front, and (iii) for stabilised temperature profile.

The model assumes constant saturation S_{wi} behind the displacement front. However, varying two-phase mobility during the displacement can affect pressure behaviour, so well injectivity prediction requires accounting for the overall saturation profile. Self-similar solution for displacement of water by CO_2 can be matched with the analytical model given by Eq. (20) using the technique of singular asymptotic expansions.

Another mechanism requiring two-phase formulation during CO_2 injection, which is not accounted for in this study, is mobilisation and migration of natural reservoir fines, that are detached by gas-water menisci (Chequer et al., 2020; Nguyen et al., 2022). The governing system includes the equation for motion of gas-water interface, where fines detachment occurs (Shapiro, 2015). The detachment is determined by the interaction of capillary and DLVO forces exerting the attached fine particle (Yuan and Moghanloo, 2018, 2019). The saturation variation from 1 to S_{wi} around CO_2-water front requires generalisation of the overall unsteady-state model for two-phase flow with moving interface (Shapiro, 2016, 2018). Accounting for two-phase flow with fines migration in the model Eq. (20) captures the effects of injectivity decline during CO_2 injection.

Other mechanisms contributing to formation damage and injectivity decline, triggered by J-T cooling effect, encompass salt precipitation, rock dissolution, mineral precipitation reaction, and hydrate formation (G Moghanloo et al., 2017; Ge et al., 2020; Nguyen et al., 2021; Turner et al., 2022). Adding those effects into Eq. (20) reflects the effects of formation damage on well injectivity during CO_2 storage in aquifers and depleted gas fields. The governing system includes balance equations for energy and mass of salt, methane, and chemical species. In large scale approximation, the hyperbolic system of the quasi-linear equations contains shocks of temperature, saturation, and component concentrations; the corresponding Riemann problems are self-similar (Lake, 1989; Polyanin et al., 2002; Polyanin and Zaitsev, 2003). Accounting for dissipative effects of diffusion and reaction kinetics induces the smoothening of the shocks by travelling wave solutions (Bedrikovetsky, 1993; Polîaînin and Dil'man, 1994). In several cases, the obtained analytical solutions for water displacement allow for exact and asymptotic upscaling (Cheng and Rabinovich, 2021; Rabinovich et al., 2015); numerous references for upscaling relevant to CO_2 injection are available from review (Bedrikovetsky and Borazjani, 2022). In addition, the analytical solution can be obtained for a temperature dependency of the J-T coefficient. This will introduce non-linear term $\alpha_{JT}(T)$ in coefficient A in Eq. (14). For this equation, the characteristics are straight lines. The solution along characteristics is obtained by separation of variables and is given by implicit integral in temperature.

Newton's law for steady state heat exchange with surrounding formations is widely applied in mathematical models of multi-phase multi component transport in natural reservoirs, like enhanced geothermal projects, thermal EOR, etc. The validation method developed in this work for 1D single-phase flow can be used for 1D and 2D multiphase flows in porous reservoirs.

The analytical model in Eq. (20) can be used to evaluate the risks of hydrate formation and/or rock integrity during CO_2 storage in depleted reservoirs.

8. Conclusions

This paper presents an analytical model for a 1D axi-symmetric problem, in which CO_2 is injected with constant rate and temperature into a semi-infinite porous medium saturated by gas and water. The model accounts for the Joule-Thomson effect due to "isenthalpic" expansion of the gas and quasi steady-state heat exchange - Newton's law - between the reservoir and the adjacent (over- and under-burden) layers. The exact solution leads to explicit expressions for the temperature profile. The solution shows that the temperature front lags significantly behind the CO_2 front due to instant heat exchange between the rock, connate water, and CO_2. The exact solution ahead of the front depends on initial temperature and is independent of the injected temperature. In adiabatic reservoir without heat supply from the adjacent layers, the temperature decreases from the well to a minimum value on the heat front, then jumps up across the front followed by slow increase up to the initial reservoir temperature. The heat supplied by the adjacent layers has two major impacts on the temperature profile: (1) it decelerates the penetration depth propagation, and (2) it decreases the temperature decline from the well to heat front. Also, the minimum temperature for this case is lower than at the case with no heat gain from the surrounding layers, and its position and value with time remain unchanged. We show that Newton's heat-exchange law yields tending of the temperature profile to steady-state profile as time tends to infinity; the penetration depth position stabilises. The position of the steady-state temperature strongly depends on dimensionless Joule-Thomson number A^* and the dimensionless temperature front velocity V^*. The analytical model is valid during a definite period from the beginning of injection; the higher is the distance from the injector the larger is the validity period. The results of this study have major implications for CO_2 storage in depleted gas fields and can be used as guide to quantify whether the temperature profile in the reservoir falls within the hydrate formation zone, or whether the induced temperature gradient can jeopardize the mechanical integrity of the rock.

CRediT authorship contribution statement

Christina Chesnokov: Data curation, Formal analysis, Investigation, Software, Validation, Visualization, Writing – review & editing. **Rouhi Farajzadeh:** Methodology, Supervision, Writing – original draft, Writing – review & editing. **Kofi Ohemeng Kyei Prempeh:** Data curation, Conceptualization, Formal analysis, Investigation, Methodology, Validation, Writing – original draft, Writing – review & editing. **Siavash Kahrobaei:** Data curation, Methodology, Validation. **Jeroen Snippe:** Project administration. **Pavel Bedrikovetsky:** Conceptualization, Writing – original draft, Writing – review & editing.

Declaration of competing interest

The authors declare that they have no known competing financial interests or personal relationships that could have appeared to influence the work reported in this paper.

Acknowledgements

The authors thank Shell Global Solutions International for permission to publish this work. Pavel Bedrikovetsky thanks Prof. K. Fedorov (Tyumen University) for fruitful discussions and ARC grant DP190103457 for support.

Appendix A. Derivation of the exact solution

Eq. (16) with BC Eqs. (18) and IC (19) present an initial-boundary value problem for a first-order partial differential equation (PDE) which is solved by the method of characteristics (Polyanin and Zaitsev, 2003). Considering the piston-like displacement of water by CO_2, two temperature domains are delineated by a shock front. First, we consider the domain ahead of the heat front, where IC propagates along the characteristic lines. Here the free variable is the dimensionless time, ς.

Assuming that, $T_D{}^*= T_D\,(x_D(\varsigma),\varsigma)$, the total derivative of $T_D{}^*$ with respect to ς is obtained as:

$$\frac{dT_D{}^*}{d\varsigma}=\frac{\partial T_D{}^*}{\partial x_D}\frac{dx_D}{d\varsigma}+\frac{\partial T_D{}^*}{\partial \varsigma}=-A^*\frac{1}{x_D}-(T_D{}^*-1) \tag{A1}$$

Therefore, the domain ahead of heat front is defined by a system of first order ODE as:

$$\frac{dx_D}{d\varsigma}=V^*;\frac{dT_D{}^*}{d\varsigma}=-A^*\frac{1}{x_D}-(T_D{}^*-1) \tag{A2}$$

The system of equations Eq. (A2) is solved with the following IC:

$$\varsigma=0: T_D{}^*=T_D(x_{D0},0)=1 \tag{A3}$$

By integrating the first part of the system of equations Eq. (A2), we obtain the trajectory of characteristics as:

$$\varsigma=\frac{x_D-x_{wD}}{V^*}-\frac{x_{D0}}{V^*} \tag{A4}$$

Further, we solve the second part of the system of equations Eq (A2) to obtain a general solution for temperature in the domain $\varsigma<\frac{x_D-x_{wD}}{V^*}$ as:

$$T_D{}^*=1-\frac{A^*}{V^*}Ei\left(\frac{x_D}{V^*}\right)e^{-\frac{x_D}{V^*}}+c_1e^{-\frac{x_D}{V^*}} \tag{A5}$$

Here, the $Ei(x)$ function is defined as:

$$Ei(x)=\int_{-\infty}^{x}\frac{e^t}{t}dt, a<b, \int_a^b\frac{e^t}{t}dt=\int_{-\infty}^{b}\frac{e^t}{t}dt-\int_{-\infty}^{a}\frac{e^t}{t}dt=Ei(b)-Ei(a) \tag{A6}$$

By using the IC Eq. (A3), the constant of integration c_1 in Eq. (A5) is obtained as:

$$c_1=\frac{A^*}{V^*}Ei\left(\frac{x_D}{V^*}-\varsigma\right) \tag{A7}$$

By substituting Eq. (A7) into the general solution Eq. (A5), the temperature profile in the domain ahead of the heat front is obtained as:

$$T_D{}^*(x_D,\varsigma)=1-\frac{A^*}{V^*}\left[Ei\left(\frac{x_D}{V^*}\right)-Ei\left(\frac{x_D}{V^*}-\varsigma\right)\right]e^{-\frac{x_D}{V^*}} \tag{A8}$$

Next, we consider the domain behind of the heat front, where BC propagates along the characteristic lines. Here the free variable is the dimensionless distance, x_D. Assuming that, $\overline{T}_D=T_D\,(x_D,\varsigma(x_D))$, the total derivative of $\overline{T}_D$ with respect to x_D is obtained as:

$$\frac{d\overline{T}_D}{dx_D}=\frac{\partial\overline{T}_D}{\partial x_D}+\frac{\partial\overline{T}_D}{\partial\varsigma}\frac{d\varsigma}{dx_D}=-\frac{A^*}{V^*}\frac{1}{x_D}-\frac{(\overline{T}_D-1)}{V^*} \tag{A9}$$

Therefore, the following system of first order ODE is obtained for the domain behind of the heat front.

$$\frac{d\varsigma}{dx_D}=\frac{1}{V^*};\frac{d\overline{T}_D}{dx_D}=-\frac{A^*}{V^*}\frac{1}{x_D}-\frac{(\overline{T}_D-1)}{V^*} \tag{A10}$$

In this domain, the system of equations Eq. (A10) is solved with the following BC:

$$x_D=x_{wD}:\overline{T}_D=T_D(x_{wD},t_{D0})=\frac{T_J}{T_I} \tag{A11}$$

By integrating the first part of the system of equations Eq. (A10), the trajectory of characteristics is:

$$\varsigma=\frac{x_D-x_{wD}}{V^*}+t_{D0} \tag{A12}$$

Additionally, we solve the second part of the system of equations Eq (A10) to obtain a general solution for temperature in the domain $\varsigma>\frac{x_D-x_{wD}}{V^*}$ as:

$$\overline{T}_D=1-\frac{A^*}{V^*}Ei\left(\frac{x_D}{V^*}\right)e^{-\frac{x_D}{V^*}}+c_2e^{-\frac{x_D}{V^*}} \tag{A13}$$

By using the BC Eq. (A11), the constant of integration c_2 in Eq. (A13) is obtained as:

$$c_2=\left(\frac{T_J-T_I}{T_I}\right)e^{\frac{x_{wD}}{V^*}}+\frac{A^*}{V^*}Ei\left(\frac{x_{wD}}{V^*}\right) \tag{A14}$$

By substituting Eq. (A14) into the general solution Eq. (A13), the temperature profile in the domain behind the heat front is obtained as:

$$\overline{T}_D(x_D,\varsigma) = 1 + \left\{ \left(\frac{T_J - T_I}{T_I}\right) e^{\frac{x_{wD}}{V^*}} + \frac{A^*}{V^*}\left[Ei\left(\frac{x_{wD}}{V^*}\right) - Ei\left(\frac{x_D}{V^*}\right)\right] \right\} e^{-\frac{x_D}{V^*}} \tag{A15}$$

Finally, the shock emanates from the point (x_{wD},0) in the x_D - ς plane, which allows for the overall dimensionless solution for the problem defined by Eq. (16) with BC Eq. (18) and IC Eq. (19) to be obtained as:

$$T_D(x_D,\varsigma) = \begin{cases} 1 + \left\{ \left(\frac{T_J - T_I}{T_I}\right) e^{\frac{x_{wD}}{V^*}} + \frac{A^*}{V^*}\left[Ei\left(\frac{x_{wD}}{V^*}\right) - Ei\left(\frac{x_D}{V^*}\right)\right] \right\} e^{-\frac{x_D}{V^*}}; \varsigma > \frac{x_D - x_{wD}}{V^*} \\ 1 - \frac{A^*}{V^*}\left[Ei\left(\frac{x_D}{V^*}\right) - Ei\left(\frac{x_D}{V^*} - \varsigma\right)\right] e^{-\frac{x_D}{V^*}}; \varsigma < \frac{x_D - x_{wD}}{V^*} \end{cases} \tag{A16}$$

The substitution of the dimensionless parameters from Eqs. (8) and (17) into Eq. (A16) yields the dimensional form of the solution given by Eq. (20) in the main text.

Appendix B. Exact solution for heat exchange in the adjacent layers of semi-infinite thickness

The assumptions of the quasi 2D heat conductivity problem in adjacent layers comprise: No horizontal heat transfer, i.e., $\gamma_x = 0$; constant vertical heat conductivity $\gamma_z = \gamma_a = const$; thickness of the shale is much smaller than the thickness of the reservoir and the adjacent layers. The equation that governs heat transfer along the vertical direction in the adjacent formations above and below the reservoir is expressed in the form:

$$(\phi_a \rho_w c_w + (1-\phi_a)\rho_{sa} c_{sa}) \frac{\partial T(r,z,t)}{\partial t} = (\phi_a \gamma_w + (1-\phi_a)\gamma_{sa}) \frac{\partial^2 T(r,z,t)}{\partial z^2}; 0 < z < \infty \tag{B1}$$

Here, φ_a is adjacent layers porosity, ρ_{sa} [ML^{-3}] is adjacent layers rock density, c_{sa} [$L^2T^{-2}K^{-1}$] is the specific heat capacity of adjacent layers rock, γ_w [$MLT^{-3}K^{-1}$] is thermal conductivity of water, γ_{sa} [$MLT^{-3}K^{-1}$] is thermal conductivity of adjacent layers and z [L] is distance in the vertical direction.

Further, the thermal diffusivity during the heat transfer is defined as:

$$a_a = \frac{\phi_a \gamma_w + (1-\phi_a)\gamma_{sa}}{\phi_a \rho_w c_w + (1-\phi_a)\rho_{sa} c_{sa}} = \frac{\gamma_a}{\phi_a \rho_w c_w + (1-\phi_a)\rho_{sa} c_{sa}} \tag{B2}$$

Substituting Eq. (B2) into Eq. (B1), the heat transfer equation is reformulated to the form:

$$\frac{\partial T(r,z,t)}{\partial t} = a_a \frac{\partial^2 T(r,z,t)}{\partial z^2} \tag{B3}$$

The initial condition (IC) corresponding to the equality of temperature in all formations is given as:

$$T(r,z,t=0) = T_I \tag{B4}$$

The boundary conditions (BC) for the semi-infinite vertical domain at infinity is that there the temperature remains equal to the initial temperature:

$$T(r,z\to\infty,t) = T_I \tag{B5}$$

The boundary condition on the shale-adjacent layer surface $z = 0$ corresponds to heat flux continuity:

$$\frac{\partial T}{\partial z}(r,z=0,t) = -\frac{\gamma_s}{\gamma_a}\frac{1}{l}[T(r=const,t) - T(r,z=0,t)] \tag{B6}$$

Here, γ_s denotes the overall shale heat conductivity and it is given as:

$$\gamma_s = \phi_s \gamma_w + (1-\phi_s)\gamma_{ss} \tag{B7}$$

Also, $T(r=const,t)$ denotes the temperature in the reservoir post injection (taken at constant radial distances from injection well).

To transform BC (B6) into dimensionless form, we introduce parameter ω:

$$\omega = \sqrt{\frac{[(1-\phi)\rho_s c_s + \phi(1-S_{wi})\rho_f c_f + \phi S_{wi}\rho_w c_w]\gamma_s h}{[(1-\phi_a)\rho_{sa} c_{sa} + \phi_a \rho_w c_w]\gamma_a l}} \tag{B8}$$

Consider the following dimensionless variables to nondimensionalize Eqs. (B3 - B6):

$$t_D = \frac{t}{t_j}; \varsigma = Bt_D; z_D = \frac{z}{\sqrt{\frac{a_a t_j}{B}}}; \theta = \frac{T}{T_I} \tag{B9}$$

Substituting Eq. (B9), and dimensionless reservoir temperature solution in Eq. (A16) into Eqs. (B3-B6) results in the dimensionless form:

$$\frac{\partial \theta}{\partial \varsigma} = \frac{\partial^2 \theta}{\partial {z_D}^2}; 0 < z_D < \infty \tag{B10}$$

$$\theta(z_D, \varsigma = 0) = 1 \tag{B11}$$

$$\theta(z_D \to \infty, \varsigma) = 1 \tag{B12}$$

$$\frac{\partial \theta}{\partial z_D}(z_D = 0) - \omega\theta(z_D = 0) = -\omega T_D(x_D = const) \tag{B13}$$

The details of the solution to the problem defined by Eqs. (B10 - B13) is expounded in the work of Polyanin and Nazaikinskii (2016). Based on the approach discussed in their work, the general solution to the second order problems of this kind is obtained as:

$$\theta(z_D, \varsigma) = \int_0^\infty f(x) G(z_D, x, \varsigma) dx - \int_0^\infty g(\tau) G(z_D, x, \varsigma - \tau) d\tau \tag{B14}$$

Here, $f(x)$ and $g(\tau)$ are arbitrary functions of x and τ, respectively and the function $G(z_D,x,\varsigma)$ is defined as:

$$G(z_D, x, \varsigma) = \frac{1}{2\sqrt{\pi\varsigma}} \left\{ e^{-\frac{(z_D - x)^2}{4\varsigma}} + e^{-\frac{(z_D + x)^2}{4\varsigma}} - 2\omega \left[\sqrt{\pi\varsigma}\, e^{\omega^2\varsigma + \omega(z_D + x)} erfc\left(\frac{z_D + x}{2\sqrt{\varsigma}} + \omega\sqrt{\varsigma} \right) \right] \right\} \tag{B15}$$

$$G(z_D, x = 0, \varsigma - \tau) = \frac{1}{\sqrt{\pi(\varsigma - \tau)}} \left\{ e^{-\frac{z_D{}^2}{4(\varsigma - \tau)}} - \omega \left[\sqrt{\pi(\varsigma - \tau)}\, e^{\omega^2(\varsigma - \tau) + \omega z_D} erfc\left(\frac{z_D}{2\sqrt{(\varsigma - \tau)}} + \omega\sqrt{(\varsigma - \tau)} \right) \right] \right\} \tag{B16}$$

From the general solution given by Eq. (B14), together with Eqs. (B15 - B16), the solution to the heat transfer problem Eqs. (B10 - B13) is obtained as:

$$\begin{aligned} \theta(z_D, \varsigma) &= erf\left(\frac{z_D}{2\sqrt{\varsigma}} \right) + e^{\omega^2\varsigma + \omega z_D} erfc\left(\frac{z_D}{2\sqrt{\varsigma}} + \omega\sqrt{\varsigma} \right) + \ldots \\ \ldots &+ \omega \int_0^\varsigma \frac{T_D(x_D = const, \tau)}{\sqrt{\pi(\varsigma - \tau)}} \left\{ e^{-\frac{z_D{}^2}{4(\varsigma - \tau)}} - \omega \left[\sqrt{\pi(\varsigma - \tau)}\, e^{\omega^2(\varsigma - \tau) + \omega z_D} erfc\left(\frac{z_D}{2\sqrt{\varsigma - \tau}} + \omega\sqrt{\varsigma - \tau} \right) \right] \right\} d\tau \end{aligned} \tag{B17}$$

The value for temperature on the interface between an adjacent layers and shale is obtained by setting z_D=0 in Eq. (B17) to obtain:

$$\theta(z_D = 0, \varsigma) = e^{\omega^2\varsigma} erfc\left(\omega\sqrt{\varsigma} \right) + \omega \int_0^\varsigma \frac{T_D(x_D = const, \tau)}{\sqrt{\pi(\varsigma - \tau)}} \left\{ 1 - \omega \left[\sqrt{\pi(\varsigma - \tau)}\, e^{\omega^2(\varsigma - \tau)} erfc\left(\omega\sqrt{\varsigma - \tau} \right) \right] \right\} d\tau \tag{B18}$$

where,

$$T_D(x_D = const, \tau) = \begin{cases} 1 + \left\{ \left(\frac{T_J - T_I}{T_I} \right) e^{\frac{x_{wD}}{V^*}} + \frac{A^*}{V^*} \left[Ei\left(\frac{x_{wD}}{V^*} \right) - Ei\left(\frac{x_D}{V^*} \right) \right] \right\} e^{-\frac{x_D}{V^*}}; \tau > \frac{x_D - x_{wD}}{V^*} \\ 1 - \frac{A^*}{V^*} \left[Ei\left(\frac{x_D}{V^*} \right) - Ei\left(\frac{x_D}{V^*} - \tau \right) \right] e^{-\frac{x_D}{V^*}}; \tau < \frac{x_D - x_{wD}}{V^*} \end{cases} \tag{B19}$$

References

Ahmadi, M.A., Chen, Z., 2019. Analytical Model for Leakage Detection in CO2 Sequestration in Deep Saline Aquifers: application to ex Situ and in Situ CO2 Sequestration Processes. ACS. Omega 4 (25), 21381–21394. https://doi.org/10.1021/acsomega.9b02668.

Alvarez, A., Bedrikovetsky, P., Hime, G., Marchesin, A., Marchesin, D., Rodrigues, J., 2005. A fast inverse solver for the filtration function for flow of water with particles in porous media. Inverse Probl. 22 (1), 69.

Alvarez, A.C., Hime, G., Marchesin, D., Bedrikovetsky, P.G., 2007. The inverse problem of determining the filtration function and permeability reduction in flow of water with particles in porous media. Transp. Porous. Media 70, 43–62.

Atkinson, P.G., Ramey Jr., H.J., 1977. Problems Of Heat Transfer. In: *Porous Media* SPE Annual Fall Technical Conference and Exhibition. https://doi.org/10.2118/6792-MS.

Battashi, M., Farajzadeh, R., Bimani, A., Al Abri, M., Mjeni, R., Karpan, V., Fadili, A., van Wunnik, J., 2022. Insights into oil recovery mechanism by Nothing-Alternating-Polymer (NAP) concept. J. Petrol. Sci. Eng. 211, 110114 https://doi.org/10.1016/j.petrol.2022.110114.

Batycky, R.P., Brenner, H., 1997. Thermal macrotransport processes in porous media. A review. Adv. Water. Resour. 20 (2), 95–110. https://doi.org/10.1016/S0309-1708(97)89141-5.

Bedrikovetsky, P., 1993. Mathematical Theory of Oil & Gas Recovery. Springer Science & Business Media. Springer Science & Business Media. https://doi.org/10.1007/978-94-017-2205-6.

Bedrikovetsky, P., Borazjani, S., 2022. Exact Solutions for Gravity-Segregated Flows in Porous Media. Mathematics (14), 10.

Celia, M.A., Nordbotten, J.M., Court, B., Dobossy, M., Bachu, S., 2011. Field-scale application of a semi-analytical model for estimation of CO2 and brine leakage along old wells. Int. J. Greenh. Gas Control 5 (2), 257–269. https://doi.org/10.1016/j.ijggc.2010.10.005.

Cermak, V., Rybach, L., 1982. Thermal Conductivity and Specific Heat of Minerals and Rocks, Subvolume A. Subvolume A, pp. 305–343. https://doi.org/10.1007/10201894_62.

Cheng, K.B., Rabinovich, A., 2021. Optimization-based upscaling for gravity segregation with 3D capillary heterogeneity effects. J. Hydrol. 603, 127062 https://doi.org/10.1016/j.jhydrol.2021.127062.

Chequer, L., Bedrikovetsky, P., Badalyan, A., Gitis, V., 2020. Water level and mobilisation of colloids in porous media. Adv. Water. Resour. 143, 103670 https://doi.org/10.1016/j.advwatres.2020.103670.

Fedorov, K.M., Sharafutdinov, R.F., 1989. Contribution to the theory of nonisothermal flow through porous media with phase transitions. Fluid Dyn. 24 (5), 721–727. https://doi.org/10.1007/BF01051725.

R. Moghanloo, G., Yan, X., Law, G., Roshani, S., Babb, G., Herron, W., 2017. Challenges Associated with CO2 Sequestration and Hydrocarbon Recovery. Recent Advances in Carbon Capture and Storage, p. 209. https://doi.org/10.5772/67226. pp.

Gao, M., Wang, L., Chen, X., Wei, X., Liang, J., Li, L., 2021. Joule–Thomson Effect on a CCS-Relevant (CO2 + N2) System. ACS. Omega 6 (14), 9857–9867. https://doi.org/10.1021/acsomega.1c00554.

Ge, J., Zhang, X., Othman, F., Wang, Y., Roshan, H., Le-Hussain, F., 2020. Effect of fines migration and mineral reactions on CO2-water drainage relative permeability. Int. J. Greenh. Gas Control 103, 103184. https://doi.org/10.1016/j.ijggc.2020.103184.

Gordeev, Y.I., Kudryashov, N.A., Murzenko, V.V., 1987. Flow regimes with temperature extrema is the motion of a gas through a porous medium. Fluid Dyn.s 22 (4), 553–559. https://doi.org/10.1007/BF01051419.

Hamza, A., Hussein, I.A., Al-Marri, M.J., Mahmoud, M., Shawabkeh, R., Aparicio, S., 2021. CO2 enhanced gas recovery and sequestration in depleted gas reservoirs: a review. J. Petrol. Sci. Eng. 196, 107685 https://doi.org/10.1016/j.petrol.2020.107685.

Hashish, R.G., Zeidouni, M., 2022. CO2 zonal injection rate allocation and plume extent evaluation through wellbore temperature analysis. Adv. Water. Resour. 164, 104203.

Jang, M., Chun, T.S., An, J., 2022. An Analytical Heat Transfer Model in Oil Reservoir during Long-Term Production. Energies (7), 15.

Kacimov, A., Obnosov, Y., 2023a. Analytical and HYDRUS solutions for exfiltration through inclined seepage faces. Adv. Water. Resour. 179, 104517 https://doi.org/10.1016/j.advwatres.2023.104517.

Kacimov, A., Obnosov, Y., 2023b. Phreatic seepage around a rectilinear cutoff wall: the Zhukovsky-Vedernikov-Polubarinova-Kochina dispute revisited. Adv. Water. Resour. 173, 104367 https://doi.org/10.1016/j.advwatres.2023.104367.

Katzourakis, V.E., Chrysikopoulos, C.V., 2019. Two-site colloid transport with reversible and irreversible attachment: analytical solutions. Adv. Water. Resour. 130, 29–36. https://doi.org/10.1016/j.advwatres.2019.05.026.

Labus, M., Labus, K., 2018. Thermal conductivity and diffusivity of fine-grained sedimentary rocks. J. Therm. Anal. Calorim. 132 (3), 1669–1676. https://doi.org/10.1007/s10973-018-7090-5.

LaForce, T., Ennis-King, J., Paterson, L., 2014. Semi-analytical solutions for nonisothermal fluid injection including heat loss from the reservoir: part 1. Saturation and temperature. Adv. Water. Resour. 73, 227–241. https://doi.org/10.1016/j.advwatres.2014.08.008.

Lake, L.W., 1989. Enhanced Oil Recovery. Prentice Hall Englewood Cliffs, N.J.

Lawal, K.A., 2020. Applicability of heat-exchanger theory to estimate heat losses to surrounding formations in a thermal flood. J. Petrol. Explor. Prod. Technol. 10 (4), 1565–1574. https://doi.org/10.1007/s13202-019-00792-5.

Machado, M.V.B., Delshad, M., Sepehrnoori, K., 2023. Injectivity assessment for CCS field-scale projects with considerations of salt deposition, mineral dissolution, fines migration, hydrate formation, and non-Darcy flow. Fuel 353, 129148. https://doi.org/10.1016/j.fuel.2023.129148.

Mathias, S.A., Gluyas, J.G., Oldenburg, C.M., Tsang, C.-F., 2010. Analytical solution for Joule–Thomson cooling during CO2 geo-sequestration in depleted oil and gas reservoirs. Int. J. Greenh. Gas Control 4 (5), 806–810. https://doi.org/10.1016/j.ijggc.2010.05.008.

Miri, R., van Noort, R., Aagaard, P., Hellevang, H., 2015. New insights on the physics of salt precipitation during injection of CO2 into saline aquifers. Int. J. Greenh. Gas Control 43, 10–21. https://doi.org/10.1016/j.ijggc.2015.10.004.

Moghadasi, J., Müller-Steinhagen, H., Jamialahmadi, M., Sharif, A., 2004. Model study on the kinetics of oil field formation damage due to salt precipitation from injection. J. Petrol. Sci. Eng. 43 (3), 201–217. https://doi.org/10.1016/j.petrol.2004.02.014.

Moreno, Z., Anto-Darkwah, E., Rabinovich, A., 2021. Semi-Analytical Modeling of Rate-Dependent Relative Permeability in Heterogeneous Formations. Water. Resour. Res. 57 (4), e2021WR029710 https://doi.org/10.1029/2021WR029710.

Moreno, Z., Rabinovich, A., 2021a. Evaluating numerical simulation errors of CO2-brine flow with capillary heterogeneity using a 1D semi-analytical solution. Int. J. Greenh. Gas Control 110, 103416. https://doi.org/10.1016/j.ijggc.2021.103416.

Moreno, Z., Rabinovich, A., 2021b. Impact of Sub-core-scale Heterogeneity on Meter-Scale Flow and Brine Displacement in Drainage by CO2. Water. Resour. Res. 57 (1), e2020WR028332 https://doi.org/10.1029/2020WR028332.

Muradov, K., Davies, D., 2012. Linear non-adiabatic flow of an incompressible fluid in a porous layer – Review, adaptation and analysis of the available temperature models and solutions. J. Petrol. Sci. Eng. 86-87, 1–14. https://doi.org/10.1016/j.petrol.2012.03.011.

Muradov, K.M., & Davies, D.R. (2009). *Temperature Modeling and Analysis of Wells with Advanced Completion* EUROPEC/EAGE Conference and Exhibition, https://doi.org/10.2118/121054-MS.

Nguyen, C., Loi, G., Russell, T., Mohd Shafian, S.R., Zulkifli, N.N., Chee, S.C., Razali, N., Zeinijahromi, A., Bedrikovetsky, P., 2022. Well inflow performance under fines migration during water-cut increase. Fuel 327, 124887. https://doi.org/10.1016/j.fuel.2022.124887.

Nguyen, M.C., Dejam, M., Fazelalavi, M., Zhang, Y., Gay, G.W., Bowen, D.W., Spangler, L.H., Zaluski, W., Stauffer, P.H., 2021. Skin factor and potential formation damage from chemical and mechanical processes in a naturally fractured carbonate aquifer with implications to CO2 sequestration. Int. J. Greenh. Gas Control 108, 103326. https://doi.org/10.1016/j.ijggc.2021.103326.

Norouzi, A.M., Niasar, V., Gluyas, J.G., Babaei, M., 2022. Analytical Solution for Predicting Salt Precipitation During CO2 Injection Into Saline Aquifers in Presence of Capillary Pressure. Water. Resour. Res. 58 (6), e2022WR032612 https://doi.org/10.1029/2022WR032612.

Oldenburg, C.M., 2007. Joule-Thomson cooling due to CO2 injection into natural gas reservoirs. Energy Conversion and Management 48 (6), 1808–1815. https://doi.org/10.1016/j.enconman.2007.01.010.

Othman, F., Naufaliansyah, M.A., Hussain, F., 2019. Effect of water salinity on permeability alteration during CO_2 sequestration. Adv. Water. Resour. 127, 237–251. https://doi.org/10.1016/j.advwatres.2019.03.018.

Parvan, A., Jafari, S., Rahnama, M., Norouzi-Apourvari, S., Raoof, A., 2021. Insight into particle detachment in clogging of porous media; a pore scale study using lattice Boltzmann method. Adv. Water. Resour. 151, 103888 https://doi.org/10.1016/j.advwatres.2021.103888.

Payne, L.E., Straughan, B., 1998. Structural stability for the Darcy equations of flow in porous media. Proc. R. Soc. Lond. *Series A: Math., Phys. Eng. Sci.* 454 (1974), 1691–1698. https://doi.org/10.1098/rspa.1998.0227.

Pires, A.P., Bedrikovetsky, P.G., Shapiro, A.A., 2006. A splitting technique for analytical modelling of two-phase multicomponent flow in porous media. J. Petrol. Sci. Engineering 51 (1), 54–67. https://doi.org/10.1016/j.petrol.2005.11.009.

Polîaînin, A.D., Dil'man, V.V., 1994. Methods of Modeling Equations and Analogies in Chemical Engineering. CRC Press Boca Raton, Fl.

Polyanin, A., Kutepov, A.M., Vyaz'min, A., Kazenin, D.A., 2002. Hydrodynamics, Mass and Heat Transfer in Chemical Engineering. CRC Press. CRC Press.

Polyanin, A., Nazaikinskii, V., 2016. Handbook of Linear Partial Differential Equations For Engineers and Scientists, Second Edition, Chapman and Hall/CRC. Chapman and Hall/CRC. https://doi.org/10.1201/b19056.

Polyanin, A., Zaitsev, V., 2003. Handbook of Nonlinear Partial Differential Equations, CHAPMAN & HALL/CRC PRESS. CHAPMAN & HALL/CRC PRESS. https://doi.org/10.1201/9780203489659.

Rabinovich, A., Itthisawatpan, K., Durlofsky, L.J., 2015. Upscaling of CO2 injection into brine with capillary heterogeneity effects. J. Petrol. Sci. Eng. 134, 60–75. https://doi.org/10.1016/j.petrol.2015.07.021.

Robertson, E.C. (1988). *Thermal properties of rocks* [Report](88-441). (Open-File Report, Issue. U. S. G. Survey. https://pubs.usgs.gov/publication/ofr88441.

Schoen, J., 2015. Physical Properties of Rocks - Fundamentals and Principles of Petrophysics, 2nd Edition ed. Elsevier.

Shapiro, A.A., 2015. Two-Phase Immiscible Flows in Porous Media: the Mesocopic Maxwell–Stefan Approach. Transp. Porous. Media 107 (2), 335–363. https://doi.org/10.1007/s11242-014-0442-0.

Shapiro, A.A., 2016. Mechanics of the Separating Surface for a Two-Phase Co-current Flow in a Porous Medium. Transp. Porous. Media 112 (2), 489–517. https://doi.org/10.1007/s11242-016-0662-6.

Shapiro, A.A., 2018. A Three-Dimensional Model of Two-Phase Flows in a Porous Medium Accounting for Motion of the Liquid–Liquid Interface. Transp. Porous. Media 122 (3), 713–744. https://doi.org/10.1007/s11242-018-1023-4.

Tsar, M., Ghasemiziarhani, M., Ofori, K., Bahrami, H., Iglauer, S., 2013. The Effect of Well Orientation (Vertical vs. Horizontal) on CO2 Sequestration in a Water Saturated Formation-saline Aquifer in Western Australia-(SPE-164935). In: 75th EAGE Conference & Exhibition incorporating SPE EUROPEC 2013.

Turner, L.G., Dawson, G.K.W., Golding, S.D., Pearce, J.K., 2022. CO2 and NOx reactions with CO2 storage reservoir core: nOx dissolution products and mineral reactions. Int. J. Greenh. Gas Control 120, 103750. https://doi.org/10.1016/j.ijggc.2022.103750.

Van der Velde, R., Mieog, J., Breunese, J., Remmelts, G., 2008. Potential For CO2 Storage in Depleted Gas Fields On the Dutch Continental Shelf. Phase 1. Technical assessment.

Vilarrasa, V., Rutqvist, J., 2017. Thermal effects on geologic carbon storage. Earth-Sci. Rev. 165, 245–256. https://doi.org/10.1016/j.earscirev.2016.12.011.

Vinogradov, A., Krasil'Shchik, I, 1999. Symmetries and Conservation Laws for Equations of Mathematical Physics. *Translations of Mathematical Monographs, American Mathematical Society 182* (Vol. 182). American Mathematical Society.

Voronov, V.P., Gorodetskii, E.E., Podnek, V.E., Grigoriev, B.A., 2016. Properties of equilibrium carbon dioxide hydrate in porous medium. Chem. Phys. 476, 61–68. https://doi.org/10.1016/j.chemphys.2016.05.031.

Xu, A., Mu, L., Fan, Z., Wu, X., Zhao, L., Bo, B., Xu, T., 2013. Mechanism of heavy oil recovery by cyclic superheated steam stimulation. J. Petrol. Sci. Eng. 111, 197–207. https://doi.org/10.1016/j.petrol.2013.09.007.

Yortsos, Y.C., Gavalas, G.R., 1982. Heat transfer ahead of moving condensation fronts in thermal oil recovery processes. Int. J. Heat. Mass Transf. 25 (3), 305–316. https://doi.org/10.1016/0017-9310(82)90183-1.

Yu, M., Hussain, F., Arns, J.Y., Bedrikovetsky, P., Genolet, L., Behr, A., Kowollik, P., Arns, C.H., 2018. Imaging analysis of fines migration during water flow with salinity alteration. Adv. Water. Resour. 121, 150–161. https://doi.org/10.1016/j.advwatres.2018.08.006.

Yuan, B., Moghanloo, R.G., 2018. Nanofluid precoating: an effective method to reduce fines migration in radial systems saturated with two mobile immiscible fluids. SPE J. 23 (03), 998–1018. https://doi.org/10.2118/189464-PA.

Yuan, B., Moghanloo, R.G., 2019. Analytical modeling nanoparticles-fines reactive transport in porous media saturated with mobile immiscible fluids. AIChE J. 65 (10), e16702. https://doi.org/10.1002/aic.16702.

Zazovskii, A.F., 1983. Nonisothermal displacement of oil by water from thermally noninsulated strata. Fluid Dyn. 18 (5), 734–741. https://doi.org/10.1007/BF01090996.

Zhang, H., Malgaresi, G., Bedrikovetsky, P., 2018. Exact solutions for suspension-colloidal transport with multiple capture mechanisms. Int. J. Non. Linear. Mech. 105, 27–42.

Ziabakhsh-Ganji, Z., Kooi, H., 2014. Sensitivity of Joule–Thomson cooling to impure CO2 injection in depleted gas reservoirs. Appl. Energy 113, 434–451. https://doi.org/10.1016/j.apenergy.2013.07.059.

Zolotukhin, A.B., 1979. In: *Analytical Definition Of The Overall Heat Transfer Coefficient* SPE California Regional Meeting. https://doi.org/10.2118/7964-MS.